$$M \to (x, y) \qquad\qquad M' \to (x + u, x + v)$$

$$N \to (x + \Delta x, y + \Delta y) \qquad N' \to (x + u + \Delta x + \Delta u, y + v + \Delta y + \Delta v)$$

These expressions become too complicated to express unless we define them in terms of strains. To express displacements in strain, we assume that the displacements are small. Otherwise, the specific dimensions that are lost in converting to strains will be necessary for a reasonable description of the shape change. The four parameters that separately describe the types of shape changes in Fig. 1.2 are the strains

$$e_{11} \text{ or } e_{xx} = \frac{\Delta u}{\Delta x} \qquad\qquad e_{12} \text{ or } e_{xy} = \frac{\Delta u}{\Delta y}$$

$$e_{21} \text{ or } e_{yx} = \frac{\Delta v}{\Delta x} \qquad\qquad e_{22} \text{ or } e_{yy} = \frac{\Delta v}{\Delta y}$$

If limits are taken, these strains can be represented by a single term describing multiaxial strain at a point as

$$e_{ij} = \frac{du_i}{dx_j} \tag{1.3}$$

or

$$du_i = e_{ij} dx_j$$

The subscript i represents the direction of displacement, and j is related to the direction of the original length that was distorted by the deformation. The total displacements can be written in terms of the original position and these strains by

$$u = e_{11}x + e_{12}y$$

$$v = e_{21}x + e_{22}y$$

We can then separate the components of the strain. The strains e_{11} and e_{22} are the tensile or compressive strains in the respective x- and y-directions. The shear strains represent distortions that include a combined shape change and rotation. The shear strains can be represented as angles of rotation by the tangent of the angular change. For small angular changes,

$$\tan \alpha \approx \frac{\Delta u}{\Delta y} = e_{12} \approx \alpha$$

$$\tan \beta \approx \frac{\Delta v}{\Delta x} = e_{21} \approx \beta \tag{1.4}$$

where α and β are expressed in radians. Unfortunately, the tensor e_{ij} measures not only distortions and rotations resulting from deformation, but also rotations that take place without any deformation. The values can be defined as a matrix or *tensor*

$$e_{ij} = \begin{vmatrix} e_{11} & e_{12} \\ e_{21} & e_{22} \end{vmatrix}$$

We can separate this tensor e_{ij} into

$$e_{ij} = \varepsilon_{ij} + \omega_{ij}$$
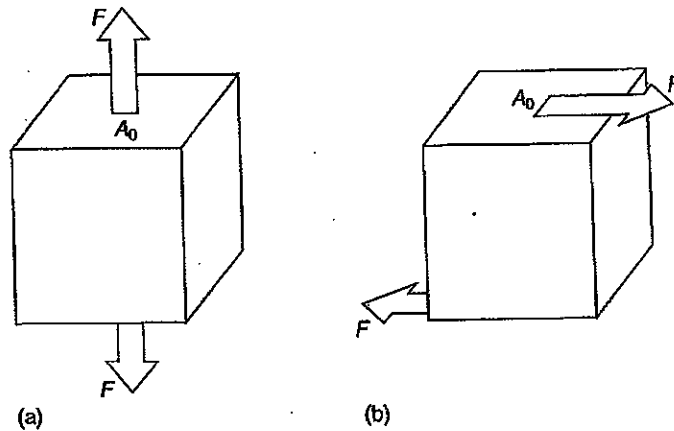
(a)   (b)

FIG. 1.5 (a) A normal tensile stress and (b) a state of shear stress (without the equal and opposite force couple required to prevent rotational acceleration).

— for plastic deformation

where A is the instantaneous area. The true stress can also be given in terms of a limit for small elements of area. Often an assumption of constant volume can be made so that

$$A_i l_i = A_f l_f$$

where A_i is the initial area, l_i is the initial length, A_f is the final area, and l_f is the final length. The true stress can then be defined in terms of the engineering stress and engineering strain as

$$\sigma_{true} = \sigma_{eng}\left(1 + e_{eng}\right)$$

1.2.2 Multiaxial Stresses

A shear stress is easily represented by a pair of force couples, of the type shown in Fig. 1.5b. If all forces are equal, there should be no net acceleration. The shear stress is defined by a force applied within the planar faces of area A.

The *shear stress* is

$$\tau = \frac{F}{A} \tag{1.10}$$

where F is a force couple applied across A (remember that an additional couple with an opposite sense is required to prevent rotational acceleration).

Most mechanical testing strategies are designed to make the relation between applied stress and the resulting strains as simple as possible. Few load-bearing components undergo only simple uniaxial stresses. Often the stress state is at least biaxial and varies with position in the part. For a defined, infinitesimal location within a component, the stress state can be defined using the two-dimensional or plane stress element shown in Fig. 1.6. Although most stress states are three-dimensional, many of the examples examined in elementary mechanics are given in terms of plane stress for simplicity. Stress states, including shear in three dimensions, can be expressed using nine terms just as we have seen for strain. Fortunately, we will demonstrate in Chapter 2 that even the most complex stress states can be simplified to three normal tensile or compressive stresses if the proper orientation frame is chosen.

brittle ceramics, glasses, and polymers. Additionally, the added expense of making tensile specimens, as well as gripping problems, often result in the use of bending as a mode for mechanical testing.

Three- and Four-Point Bending   Two bending geometries are common for low-temperature and high-temperature strength and fracture toughness measurements. Three- and four-point loading geometries are shown in Fig. 1.10. In strength tests, the maximum tensile stress in the bend specimen at failure is often termed the *modulus of rupture*. For elastic loading, the expressions for the maximum stress are given as

$$\sigma_{max} = \frac{Plh}{8I}$$

(1.12)

for three-point bending and

$$\sigma_{max} = \frac{Plh}{4I}$$

(1.13)

for four-point bending. In both equations, P is the applied force, l is the spacing between the two outer loading points in three-point bending, h is the specimen height, and I is the moment of inertia. In four-point bending, the inner loading points are designated by l. The moment of inertia for bend specimens with uniform rectangular cross sections is given by

$$I = \frac{wh^3}{12}$$

(1.14)

where w is the sample width. The stress varies linearly across the specimen height for specimens with rectangular cross sections. For a circular cross section, the diameter d is used for the moment of inertia $(d$ replaces h in bending equations$)$

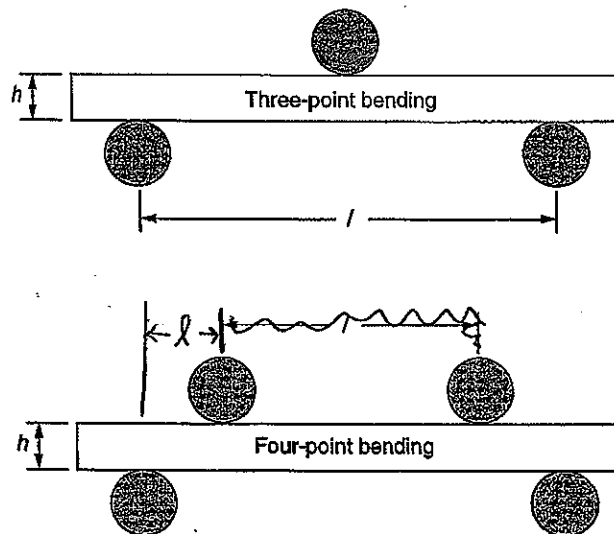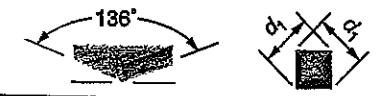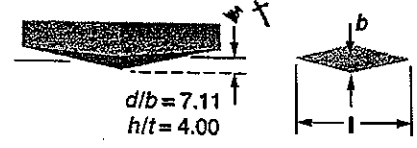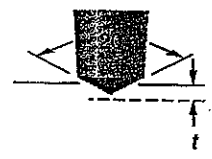$$I = \frac{\pi d^4}{64}$$

(1.15)

FIG. 1.10 Geometry for three-point and four-point bend tests.

TABLE 1.1   Parameters for the Most Common Rockwell Hardness Tests and the Corresponding Indenter Shapes*

Vickers	Diamond pyramid			P
Knoop microhardness	Diamond pyramid	$d/b = 7.11$ $h/t = 4.00$		P
Rockwell				
A C D	Diamond cone			60 kg 130 kg 100 kg
B F G	$\frac{1}{16}$-in.– diameter steel sphere			100 kg 60 kg 150 kg
E H	$\frac{1}{4}$-in.– diameter steel sphere			100 kg 60 kg

Source: Adapted from Callister, 1996, Wiley, used with permission.

*The A, C, and D tests are calculated using 100–500t = Rockwell number, with t being depth of penetration in microns. The B, F, G, E, and H tests are calculated using 130–500t = Rockwell number, with t being depth of penetration in microns.

The Knoop indenter is a pyramidal diamond indenter that produces an indentation with long and short diagonals in a ratio of 7:1. The Knoop Hardness Number (KHN) is given as

$$KHN = \frac{CP}{L^2}$$

(1.18)

where P is load in kilograms, L is long diagonal length in millimeters, and C is a constant for a specific indenter, typically 14.2.

1.3.4 Fracture Toughness

The resistance of a material to the propagation of a crack under a stress applied normal to the crack plane is defined as the fracture toughness K_{Ic}. The theoretical value of the fracture toughness of a brittle material is defined as

$$K_{Ic} = \sqrt{EG}$$

(1.19)

where E is Young's modulus and G is called the critical strain energy release rate. For a brittle material, $G = 2\gamma$, where γ is the surface energy. For ductile materials, $G > 2\gamma$. Direct determination of solid surface energies is very difficult. Thus, mechanical tests are conducted on samples with known preexisting flaws. The specimen and loading geometries

TABLE 1.4 Fracture Behaviors of Various Materials at Room Temperature*

Material	Ultimate tensile strength (UTS) (MPa)	Fracture toughness, K_{Ic} (MPa · m$^{1/2}$)
Aluminum alloys	100–800	20–60
Copper alloys	200–1000	140–120
Iron alloys and steels	250–2000	10–200
Stainless steels	300–700	50–200
Titanium alloys	300–1300	40–120
Aluminum oxide	200–600	3–5
Silicon carbide	250–600	2–5
Glass	70–200	0.5–1.5
Polyethylenes (PE)	20–100	2–6
Polymethylmethacrylate (PMMA)	40–120	1–3
Polystyrene (PS)	40–100	1–2
Bone	60–150	2–10
Tendon	45–50	—

*Data in this table are often meaningful only for K_{Ic} values less than 10 MPa/m$^{1/2}$. For values greater than 10 MPa/m$^{1/2}$, the component thicknesses necessary to fulfill plane strain conditions are not practical for many applications. This will be discussed further in Chapter 7.

1.5 HOW BONDING INFLUENCES MECHANICAL PROPERTIES

The nature of the bonds in materials determines the responses of the materials to applied stress as much as the melting temperature and the crystalline or molecular arrangement. The three categories of strong bonds—ionic, covalent, and metallic—comprising the bonds between atoms and ions within crystals and molecules and the secondary bonds between crystals and molecules determine the mechanical responses of materials (see Rohrer, 2001).

1.5.1 Linear Elasticity

The net result of attractive and repulsive energies, $E_T = E_{attractive} + E_{repulsive}$, for a particular bond is an asymmetric energy relationship for the spacing r between atom or ion centers shown in Fig. 1.24a. As the influence of atomic vibration increases at higher temperatures, the average spacing $\bar{r}$ increases, representing the thermal expansion shown in Fig. 1.24b. The relationship of the force F between atoms on ions with spacing is found by taking the slope dE_T/dr of the energy relationships.

Elastic properties are only defined over small strains so that the slope of the F versus r curve defining the effective spring constant for small stretches of the bonds can be treated as linear. Then, if $F = kr$, Young's modulus, E, must scale with K.

The shapes of the energy and force curves in Fig. 1.24 determine the stiffness of the bonds. They also give the corresponding strengths of the bonds. The effects of thermal vibration have an impact on the elastic stiffness and also the thermal expansion coefficient. Young's modulus decreases with increasing temperature and the thermal expansion coefficient decreases with increasing temperature. Data for Young's modulus versus temperature are given in Fig. 1.25. Figure 1.26 shows that the elastic stiffness of the bonds indicated by the room-temperature Young's modulus scales with the melting temperature. Detailed plots

1.7 PROBLEMS

A.1.1 How do the points in the worm in Fig. 1.1 change with strain? (Think of the mathematical definition of a point.)

A.1.2 Take a string that is originally 1 m in length and stretch it in three stages.

(a) Stretch it by 0.1 m.

(b) Stretch it by an additional 0.2 m.

(c) Stretch it by an additional 0.2 m.

For each stage, calculate and compare the engineering and true strains.

A.1.3 Plot true strain versus engineering strain for stretching of a string from 1 m to 1.5 m. Plot enough points to yield a smooth curve.

A.1.4 Measure the displacements of M and N on the worm in Fig. 1.1 in millimeters. From these measurements, calculate the tensile strain in engineering strain and true strain.

A.1.5 Measure the displacements of M and N in Fig. 1.2 in millimeters. From these measurements, estimate all four strains e_{ij}.

A.1.6 Measure the displacements of the strained square in Fig. 1.3 in millimeters. From these measurements, estimate all four strains e_{ij}.

A.1.7 Show how SI units of stress can also be expressed as energy per unit volume.

A.1.8 The Brinell hardness of a new alloy is measured using a load of 3000 kg. The indentation diameter is 2 mm. What is the BHN? What is the indentation depth?

A.1.9 Calculate Young's modulus and the 0.2% offset yield stress for the stress-strain curve in Fig. 1.17.

A.1.10 Give common SI units for the following mechanical properties.

(a) Stress _____ or _____ /m²

(b) Fracture toughness _____ or _____ /m³ᐟ²

(c) Creep rate _____

(d) Yield strength _____

(e) Young's modulus _____

(f) Poisson's ratio _____

B.1.1 Assume that a rectangle plotted in the x-z plane has dimensions of 2 cm × 5 cm. Apply the following values of strain to the rectangle.

$$\begin{vmatrix} 0.1 & 0 & 0.1 \\ 0 & 0 & 0 \\ 0.3 & 0 & -0.1 \end{vmatrix}$$

Give the separate components of shape-change strain and rotational strain.

B.1.2 Write the strain tensor for $du_1 = 0.01$, $du_2 = 0.02$, $du_3 = 0.01$, $dx_1 = dx_2 = dx_3 = 1$. Describe the shape change. Describe the rotation.

B.1.3 Deform a cube by stretching it 20 percent in the x-direction and reducing it 20 percent in the y-direction. Does it maintain the same volume?

B.1.4 Assume Fig. 1.17 is a true stress–true strain plot. Replot this data and overlay it with the engineering stress-strain curve for the same data (similar to Fig. 1.18). Why are the curves so similar?

B.1.5 (a) Using Eq. 1.25, calculate the values of K and n that best fit the data for brass in Fig. 1.18.

(b) Are your values ~~similar to that predicted in the description of~~ Eq. 1.25? ⌐consistent with

(c) Estimate the strain hardening rate $d\sigma/d\varepsilon$ for this curve at the point of necking indicated on the true stress–true strain curve.

B.1.6 Use Hooke's law for multiaxial stresses to calculate the stresses required to produce the strains described in Problem B.1.3. (Assume the material is steel with a Young's modulus ≈ 210 GPa and a Poisson's ratio ≈ 0.2). Is the magnitude of the stresses too large for just elastic distortion?

B.1.7 Your nearby engineering library should have ASTM standards for mechanical testing. The standards include geometries and dimensions of typical samples. Find the correct ASTM standards for

(a) Tensile testing of metals or polymers

(b) Bend testing of ceramics

(c) Fracture testing of metals

(d) Fracture testing of ceramics.

B.1.8 Estimate the apparent linear Young's modulus for the PBT samples shown in Fig. 1.22. By finding the slope up to an engineering stress of 40MPa, predict the modulus for a sample tested at a strain rate of $3 \times 10^{-2}\ s^{-1}$.

B.1.9 Assume that a beam of square cross section is bent elastically in four-point bending. Describe the changes that would occur in the cross section between the inner loading points, and show how you would calculate the shape.

C.1.1 (a) A wooden plank with a rectangular cross section will be used to span a small stream on a hiking trail. The plank will be expected to carry one person at a time. The plank will be supported only on each end. The width of the crossing is 3 m and the plank will lie about 3 m above the stream. The maximum width of

stock available is 0.6 m. The fracture stress of the wood along the growth direction is approximately 8 MPa. Give your design for a safe crossing.

(b) The trail engineer has suggested that the possibility of two people crossing simultaneously should be considered. Show how the safe design of the crossing would change for the possibility of two people crossing together. Is the crossing safer if the two people are closer together or farther apart?

(c) The trail engineer has suggested that a round log would make a more interesting span. Limited to a maximum diameter of 0.6 m, will the log be more or less safe than your design for part (a)? *minimizing*

C.1.2 ~~Two~~ *four* materials are proposed for the same application. The most critical performance criterion is the change in thickness on loading under a biaxial stress. The proposed part is a thin plate measuring 4 mm by 4 mm by 0.1 mm. The part will undergo a biaxial tensile load of 2 MPa. For the properties given below, rank the materials from best to worst.

$$M1 - E = 200 \text{ GPa}, \nu = 0.3$$
$$M2 - E = 180 \text{ GPa}, \nu = 0.25$$
$$M3 - E = 220 \text{ GPa}, \nu = 0.32$$
$$M4 - E = 250 \text{ GPa}, \nu = 0.35$$

C.1.3 (a) Estimate the yield ~~stress~~ *strength* for the half-hard and annealed brasses in Fig. 1.20.

(b) Calculate the true stress–true strain curves for the half-hard and annealed brasses in Fig. 1.20. *(only plot the data up to the maximum on the curves, which is where localized ~~test~~ deformation begins)*

(c) Fit the data from parts (a) and (b) to Eq. 1.25. Which material has the higher strain hardening rate?

(d) For the annealed brass, fit only the data after the flow stress has reached the yield stress of the half-hard brass. ~~Why~~ *Is* the deformation *so* similar to that of the half-hard brass?

C.1.4 (a) Estimate the yield stress for all three materials in Fig. 1.21.

(b) Calculate the true stress–true strain curves for the three materials in Fig. 1.21 *(prior to necking)*.

(c) Fit the data for the two materials in the T6 condition to Eq. 1.25. Which material has the higher strain hardening rate? How does this compare with the point at which necking takes place? Estimate the engineering strain at which necking starts and calculate the corresponding true strain. Is this consistent with your expectations?

(d) For the annealed brass, fit the data up to a true strain of 0.1 to Eq. 1.25. Compare the value of n with those of the two other aluminum samples.

C.1.5 The plank bridge in Problem C.1.1(a) has collapsed as a result of a fire. The use of a steel tube has been proposed. A steel tube is available with a 1-meter outer diameter and a 1-cm wall thickness. The moment of inertia for a tube is

$$I = \frac{\pi}{64}\left(d_o^4 - d_i^4\right)$$

where d_o is the outer diameter and d_i is the inner diameter. Will these tubes safely support expected loads? Explain your answer.

TENSORS AND ELASTICITY

STRESS, STRAIN, AND ELASTICITY are most conveniently represented by tensors. Tensors and the related matrices provide an opportunity to utilize the mathematics taken through the second year of university in a very powerful approach for understanding elasticity and deformation of materials. The geometric relations given in this chapter also provide handy tools for solution of many problems related to crystals and composites. The necessity for tensors may seem obvious when one considers the properties of fiber composites, but cubic metals can show strong variations in elastic and plastic properties with the direction of applied stress. Both the student and the instructor may find that tensors are not easy to learn or to teach. If we restrict ourselves to the solutions given for uniaxial conditions or rely on equations in books for directional properties, we can solve only idealized problems. The goal of this chapter is to demonstrate the enabling capabilities derived from an understanding that tensorial relations are the foundation for physical and mechanical properties.

based

A common misconception is that cubic materials are isotropic—with all properties the same in all directions. As shown later in this chapter, many properties of cubic single crystals are isotropic, but elasticity and some similar properties called electrostriction and magnetostriction are anisotropic even in cubic materials. One very important application of single crystals is in the hotter stages of a turbine engine. The turbine blades located in this part of the engine typically consist of nickel-base single crystals grown with a specific orientation designed to resist long-term deformation. These single crystals consist of a disordered phase reinforced with cuboidal grains of an ordered compound called an intermetallic. The anisotropy of the cubic grains is demonstrated by a variation in elastic constants with direction in the material. The magnitude of this elastic anisotropy in a single crystal turbine blade can be surprisingly large, as shown by the values of Young's modulus given for specific crystallographic directions in Fig. 2.1.

Other applications of cubic single crystals with strong elastic anisotropies include silicon and gallium arsenide in microelectronics and alkali halides used for their optical properties. Figure 2.2 defines a standard cubic coordinate system with specific directions labeled. The values of Young's modulus in these low-index crystal directions are given in Table 2.1 for several cubic metals. Tensor representations enable calculation of any elastic constant in an arbitrary direction from the information given in this table. Other materials show anisotropy as a result of preferred orientation or texture of the crystals or molecules that comprise the material. Oriented materials can have strong anisotropies, as shown in Table 2.2. The magnitude of the anisotropy for many of these materials is dependent on the degree of preferred orientation. The strain and thermal history of deformation processing along with the mechanisms of deformation influence the degree of orientation and thereby the degree of anisotropy.

Although we assume a symmetric tensor such that $\sigma_{12} = \sigma_{21}$, to perform the second-rank tensor transformation using Eq. 2.7, we must use the correct subscripts for each term in the transformation

$$\sigma_{ij}' = a_{ik}a_{jl}\sigma_{kl}$$

We can then define the stresses at any orientation in the x-y plane—viz., $\sigma_{ij}' = \sigma_{ij}$ ($\phi 1$)—using the rotation matrix

$$a_{ij} = \begin{vmatrix} \cos\phi 1 & \sin\phi 1 & 0 \\ -\sin\phi 1 & \cos\phi 1 & 0 \\ 0 & 0 & 1 \end{vmatrix}$$

Then solutions for σ_{11}' and σ_{12}' are given by

$$\sigma_{11}' = \sum_{k}^{3}\sum_{l}^{3} a_{1k}a_{1l}\sigma_{kl}$$

$$\sigma_{11}' = a_{11}a_{11}\sigma_{11} + a_{11}a_{12}\sigma_{12} + a_{12}a_{11}\sigma_{21} + a_{12}a_{12}\sigma_{22}$$

$$= \cos^2\phi 1\,\sigma_{11} + 2\sin\phi 1\,\cos\phi 1\,\sigma_{12} + \sin^2\phi 1\,\sigma_{22}$$

$$\sigma_{12}' = a_{11}a_{21}\sigma_{11} + a_{11}a_{22}\sigma_{12} + a_{12}a_{21}\sigma_{21} + a_{12}a_{22}\sigma_{22}$$

$$= \sigma_{12}\left(\cos^2\phi 1 - \sin^2\phi 1\right) + \left(\sigma_{22} - \sigma_{11}\right)\sin\phi 1\,\cos\phi 1$$

Using trigonometric substitutions and setting $\sigma_{12}' = 0$, the equations for principal stress become

$$s_1, s_2, \text{ or } s_3 = \frac{\sigma_{11} + \sigma_{22}}{2} \pm \sqrt{\left(\frac{\sigma_{11} - \sigma_{22}}{2}\right)^2 + \left(\sigma_{12}\right)^2} \qquad (2.14)$$

where s_1 is the algebraically largest principal stress, s_2 the next largest, and s_3 the smallest. These values of stress are the same stresses obtained using Mohr's circle, which is defined in mechanics or strength of materials texts.

EXAMPLE 2.2 *Principal Stresses for Stress Tensors*

Two-Dimensional Stress States

For the Mohr's circle shown in Fig. 2.7, the values are given in tensor form as

$$\begin{vmatrix} 6.66 & 7.66 & 0 \\ 7.66 & -1.66 & 0 \\ 0 & 0 & 0 \end{vmatrix}\text{MPa}$$

where the principal stresses are $s_1 = 10$, $s_2 = 0$, and $s_3 = -5$.

Three-Dimensional Stress States

The principal stresses for the three-dimensional stress state given below are found by obtaining the roots of the determinant shown below. The difference between the diagonal matrix containing SP and the applied stress matrix defines a cubic equation after the determinant is taken.

$$\begin{vmatrix} \begin{pmatrix} SP & 0 & 0 \\ 0 & SP & 0 \\ 0 & 0 & SP \end{pmatrix} - \begin{pmatrix} 10 & -3 & 4 \\ -3 & 5 & 2 \\ 4 & 2 & 7 \end{pmatrix} \end{vmatrix}\text{MPa}$$

FIG. 2.7 Schematic of a Mohr's circle.
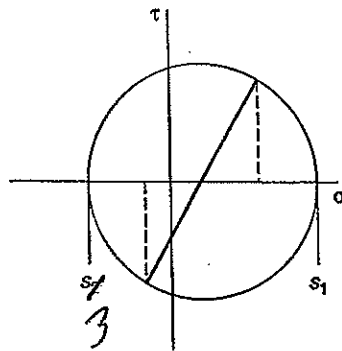
The roots of this determinant are the principal stresses.

$$s = \begin{vmatrix} 13 & 0 & 0 \\ 0 & 7.8 & 0 \\ 0 & 0 & 1.2 \end{vmatrix} \text{MPa}$$

An expression for the determinant is the cubic equation for the principal stress. We can set this equal to zero:

$$s^3 - I_1 s^2 - I_2 s - I_3 = 0$$

where I_1, I_2, and I_3 are taken from the stresses

$$\sigma = \begin{pmatrix} 10 & -3 & 4 \\ -3 & 5 & 2 \\ 4 & 2 & 7 \end{pmatrix} \text{MPa}$$

as $\quad I_1 = \sigma_{11} + \sigma_{22} + \sigma_{33}$

$I_2 = (\sigma_{12})^2 + (\sigma_{23})^2 + (\sigma_{13})^2 - \sigma_{11} \cdot \sigma_{22} - \sigma_{22} \cdot \sigma_{33} - \sigma_{11} \cdot \sigma_{33}$

$I_3 = \sigma_{11} \cdot \sigma_{22} \cdot \sigma_{33} + 2 \cdot \sigma_{12} \cdot \sigma_{23} \cdot \sigma_{13} - \sigma_{11} \cdot (\sigma_{23})^2 - \sigma_{22} \cdot (\sigma_{13})^2 - \sigma_{33} \cdot (\sigma_{12})^2$

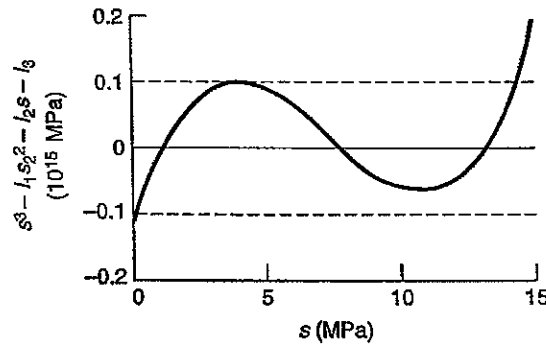The resulting function can be plotted to show the three roots, as shown in Fig. 2.8. ■

FIG. 2.8 Cubic equation of principal stresses, showing the roots $s_1 = 13$, $s_2 = 7.8$, and $s_3 = 1.2$ MPa.
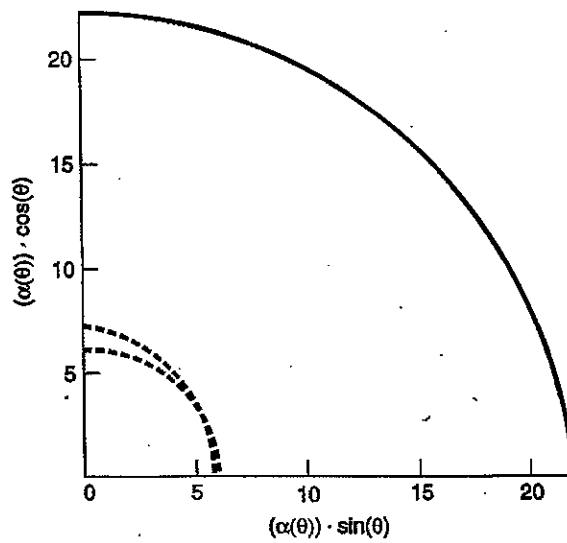
FIG. 2.11 Thermal expansion "surface" for the data plotted in Fig. 2.10 from 0 to $\pi/2$.

Then, if we use the properties of alumina (ignoring the elastic anisotropy of the sapphire), we can use Hooke's law for a biaxial stress state in a thin film ($s_1 = s_2$, $s_3 = 0$) to calculate the stresses.

$$E_{alumina} = 390 \text{ GPa} \qquad \nu_{alumina} = 0.25$$

$$s_1 = \frac{E_{alumina} \cdot \varepsilon_{mismatch}}{(1 - \nu_{alumina})} = 152 \text{ MPa}$$

TABLE 2.7   Thermal Expansion Coefficients for Materials with Different Symmetries

Material	Symmetry	Temperature °C	α_1 $(10^{-6}\,C^{-1})$	α_2 $(10^{-6}\,C^{-1})$	α_3 $(10^{-6}\,C^{-1})$
Aluminum	Random	25–100	22	22	22
Aluminum*	Cubic	25–100	22	22	22
Iron	Random	25–100	12	12	12
Iron*	Cubic	25–100	12	12	12
Silicon nitride	Random	25–100	1.8	1.8	1.8
Zinc	Random	25–100	20	20	20
Aluminum oxide	Random	25–100	6.0	6.0	6.0
Calcite	Random	25–100	4.5	4.5	4.5
Gypsum	Random	25–100	24	24	24
HDPE	Random	25–100	90	90	90
Epoxy	Random	25–100	60	60	60
Silicon nitride*	Hexagonal	100–200	1.3	1.3	2.8
Zinc*	Hexagonal	25–100	14 ~~8~~	14 ~~8~~	~~64~~ 64
Sapphire*	Rhombohedral	25–100	5.7	5.7	7
Calcite*	Rhombohedral	25–100	–5.6	–5.6	25
Gypsum*	Monoclinic	25–100	1.6	42	29
60 v/o glass fiber in epoxy	Axisymmetric‡	25–100	34	34	6
Kevlar	Axisymmetric‡	25–100	59	59	–2

* Single crystals.

‡ For axisymmetric materials, α_3 is the thermal expansion coefficient along the axis of symmetry.

BIOGRAPHY

S. D. POISSON (1781–1840)

Poisson taught undergraduate calculus and was a student of Laplace and Lagrange. Using the assumptions of Cauchy and Ostrogradsky, v should be equal to one-fourth in all isotropic solids. Thus, isotropic solids should have only one elastic constant. It was Green that demonstrated that isotropic solids should have two independent elastic constants.

where Poisson's ratio, v_{ij}, is defined as the negative of the ratio of the strain in the i-direction to the strain in the j-direction owing to an applied stress in the i-direction, yielding

$$\varepsilon_2 = -v_{12}\varepsilon_1 \quad \text{or} \quad v_{12} = \frac{-\varepsilon_2}{\varepsilon_1} \tag{2.22}$$

Another familiar quantity is Young's modulus, which can be related to principal directions by E_i, the modulus of elasticity in the i-direction. Then

$$\varepsilon_1 = S_{11}\sigma_1 = \frac{\sigma_1}{E_1}$$

$$\varepsilon_2 = S_{21}\sigma_1 = -v_{12}\varepsilon_1 = \frac{-v_{12}\sigma_1}{E_1}$$

$$\varepsilon_3 = S_{31}\sigma_1 = -v_{13}\varepsilon_1 = \frac{-v_{13}\sigma_1}{E_1}$$

and

$$S_{11} = \frac{1}{E_1} \qquad S_{21} = \frac{-v_{12}}{E_1} \qquad S_{31} = \frac{-v_{13}}{E_1}$$

For Poisson's ratio, $v_{ij} \neq v_{ji}$, because

$$v_{12} = \frac{-S_{21}}{S_{11}}$$

and we already know that $S_{12} = S_{21}$.

If we put all of this together, we can write the matrix of values for the compliances as

$$S = \begin{vmatrix} \dfrac{1}{E_1} & \dfrac{-v_{21}}{E_2} & \dfrac{-v_{31}}{E_3} & 0 & 0 & 0 \\[2mm] \dfrac{-v_{12}}{E_1} & \dfrac{1}{E_2} & \dfrac{-v_{32}}{E_3} & 0 & 0 & 0 \\[2mm] \dfrac{-v_{13}}{E_1} & \dfrac{-v_{23}}{E_2} & \dfrac{1}{E_3} & 0 & 0 & 0 \\[2mm] 0 & 0 & 0 & \dfrac{1}{M_4} & 0 & 0 \\[2mm] 0 & 0 & 0 & 0 & \dfrac{1}{M_5} & 0 \\[2mm] 0 & 0 & 0 & 0 & 0 & \dfrac{1}{M_6} \end{vmatrix} \tag{2.23}$$

$$C_{12} = \frac{-S_{12}}{(S_{11} - S_{12})(S_{11} + 2S_{12})}$$

$$C_{44} = \frac{1}{S_{44}}$$

Using the direction cosines, l, m, and n, for a particular reference direction, one can determine the elastic properties of a cubic single crystal in a particular direction by the relationship

$$\frac{1}{E_{hkl}} = S_{11}' = S_{11} - 2\left[S_{11} - S_{12} - \frac{1}{2}S_{44}\right]\left(l^2m^2 + m^2n^2 + l^2n^2\right) \qquad (2.25)$$

Table 2.8 lists C_{ij} and S_{ij} values for several cubic and hexagonal materials. Figure 2.14 shows Young's modulus surfaces for Eq. 2.25 plotted with reference to a three-dimensional coordinate system.

TABLE 2.8 Stiffness and Compliance Values for Various Crystals (at Room Temperature)

Material	C_{11}	C_{33}	C_{12}	C_{23}	C_{44} (GPa)	S_{11}	S_{33}	S_{12}	S_{23}	S_{44} (10^{-3} GPa^{-1})
Cubic										
Aluminum	108	—	61	—	28	15.7	—	−5.70	—	35.1
Copper	168	—	121	—	75.4	15.0	—	−6.30	—	13.3
Gold	186	—	157	—	42	23.3	—	−10.7	—	24
Lead	47	—	40	—	14.4	93	—	−42.4	—	69
Nickel	247	—	147	—	125	7.3	—	−2.7	—	8.0
Silver	124	—	93.4	—	46	22.9	—	−9.8	—	22
Iron .	237	—	141	—	116	8.00	—	−2.8	—	8.60
Molybdenum	460	—	176	—	110	2.8	—	−0.78	—	9.1
Niobium	246	—	134	—	28.7	6.6	—	−2.3	—	34.8
Tantalum	267 *~~510~~*	—	161	—	82.5	6.9	—	−2.6	—	12.2
Tungsten	~~500~~ *160*	—	200	—	~~140~~ *160*	2.6	—	−0.7	—	6.6
C (diamond)	1076	—	125	—	566	1.1	—	−0.22	—	2.1
Germanium	129	—	48.3	—	67.1	9.8	—	−2.7	—	15
Silicon	166	—	63.9	—	79.6	7.7	—	−2.1	—	12.6
Potassium	4.6	—	3.7	—	2.6	82	—	−370	—	380
Zinc sulfide	108	—	72	—	41	20	—	−8.00	—	24
Magnesium oxide	296	—	95	—	156	4.00	—	−1.0	—	6.5
Sodium chloride	49	—	12	—	13	23	—	−4.7	—	79
Lithium fluoride	111	—	42	—	62.8	11.1	—	−3.1	—	15.9
Titanium carbide	513	—	106	—	178	2.1	—	−0.36	—	5.61
Hexagonal										
Cadmium	121	51.3	40	41	20	~~12.9~~ *11.4*	~~36.5~~ *32.9*	~~−4.6~~ *−0.9*	~~−3.3~~ *−8.4*	~~34~~ *50*
Titanium	160	181	92	69	46.5	9.70	6.9	−4.7	−1.8	~~24.6~~ *21.5*
Zinc	161	61	34.1	50	38.3	8.4	28.4	0.5	−7.3	26.1
Magnesium	59.7	61.7	26.2	21.7	16.4	22	20	−8.0	−5.0	61

(Kelly, Groves, and Kidd, 2000, Simmons and Wang, 1971, Hirth and Lothe, 1982, and Nye, 1957)

The rotation matrix is then

$$\begin{vmatrix} 1 & 0 & 0 \\ 0 & \cos\Phi & \sin\Phi \\ 0 & -\sin\Phi & \cos\Phi \end{vmatrix}$$

leading to the following sequence of calculations for S'_{44}, where S'_{44} is the inverse shear modulus (or shear compliance) in the original coordinate system, which is related to the specimen cut at 45° by the transformation shown above.

$$S'_{44} = 4S'_{2323} = 4a_{2m}a_{3n}a_{2o}a_{3p}S_{mnop}$$

Note first that any S' values with subscripts of 1 will be zero, yielding

$$S'_{2323} = a_{22}a_{32}a_{22}a_{32}S_{2222} + a_{23}a_{33}a_{23}a_{33}S_{3333} +$$

$$a_{22}a_{32}a_{23}a_{33}S_{2233} + a_{23}a_{33}a_{22}a_{32}S_{3322} +$$

$$a_{22}a_{33}a_{22}a_{33}S_{2323} + a_{23}a_{32}a_{23}a_{32}S_{3232} +$$

$$a_{22}a_{33}a_{23}a_{32}S_{2332} + a_{23}a_{32}a_{22}a_{33}S_{3223}$$

$$= \cos^2\Phi\sin^2\Phi\, S_{2222} + \cos^2\Phi\sin^2\Phi\, S_{3333} - 2\cos^2\Phi\sin^2\Phi\, S_{2233} + \cos^4\Phi\, S_{2323} + \sin^4\Phi\, S_{3232}$$
$$- \cos^2\Phi\sin^2\Phi\, S_{3223} - \cos^2\Phi\sin^2\Phi\, S_{2332}$$

Substituting $\frac{1}{4}S_{44}$ for each of the shear components and $1 - \cos^2\Phi$ for each $\sin^2\theta$ gives the final solution

$$S'_{44} = 4S'_{2323} = 4\cos^2\Phi(1 - \cos^2\Phi)\,[S_{22} - 2S_{23} + S_{33}] + (2\cos^2\Phi - 1)^2\, S_{44}$$

Using a value of 45° for Φ, the solution is then

$$S'_{44} = [S_{22} - 2S_{23} + S_{33}]$$

which means that by measuring Poisson's ratio and Young's moduli at 45° from the z symmetry axis we can recover the shear modulus of the material. ∎

EXAMPLE 2.5 *Stiffnesses for Mo at 25°C in GPa*

Most math software and programming languages are not readily suited to tensors of greater than second rank. This example demonstrates one way to map subscripts from 4 to 2 using the definitions provided by a special matrix M. First, we can assign the proper 9 × 9 matrix of 81 terms by setting the magnitudes of the three independent elastic constants for cubic materials on their principal axes.

$$c_{11} = 460 \qquad c_{12} = 176 \qquad c_{44} = 110 \text{ (GPa)}$$

Then the 9 × 9 matrix contains these values at each appropriate position, with

$$C = \begin{bmatrix} c_{11} & c_{12} & c_{12} & 0 & 0 & 0 & 0 & 0 & 0 \\ c_{12} & c_{11} & c_{12} & 0 & 0 & 0 & 0 & 0 & 0 \\ c_{12} & c_{12} & c_{11} & 0 & 0 & 0 & 0 & 0 & 0 \\ 0 & 0 & 0 & c_{44} & 0 & 0 & c_{44} & 0 & 0 \\ 0 & 0 & 0 & 0 & c_{44} & 0 & 0 & c_{44} & 0 \\ 0 & 0 & 0 & 0 & 0 & c_{44} & 0 & 0 & c_{44} \\ 0 & 0 & 0 & c_{44} & 0 & 0 & c_{44} & 0 & 0 \\ 0 & 0 & 0 & 0 & c_{44} & 0 & 0 & c_{44} & 0 \\ 0 & 0 & 0 & 0 & 0 & c_{44} & 0 & 0 & c_{44} \end{bmatrix}$$

is applied to a unit cube. Describe the changes, in terms of changes in length and angles, that will take place in lines that were in the [111], [110], [1$\bar{1}$0], and [100] before the strain took place.

B.2.4 Two isotropic crystals, with Poisson's ratios of 0.4 and 0.6 are stretched to an elastic strain of 0.01. Describe the volume change in each material and the origins of the response. Compare the results for the exact volume strain.

B.2.5 If both the crystals in Problem B.2.4 had a Young's modulus of 2 GPa, find the tensile stress that will produce a transverse strain of 0.005. Determine the bulk and shear moduli of the two materials.

B.2.6 Plot values of Young's modulus for all possible directions in the (100), (110), and (123) for MgO. (*Hint:* Find the rotation matrix that puts the plane normal as z′ at some rotation of $\phi 1$ and ϕ and then plot Young's modulus as a function of $\phi 1$.)

B.2.7 Write the symbolic expression for C'_{13} for an arbitrary rotation of Φ for orthorhombic and cubic symmetry.

B.2.8 Find the shear modulus for shearing in the [110] on the (1$\bar{1}$2) for iron and aluminum.

B.2.9 Find Young's modulus for Germanium along [110].

(a) Complete the rotation matrix

	x	y	z
x′	$\dfrac{1}{\sqrt{2}}$	$\dfrac{1}{\sqrt{2}}$	0
y′	$\dfrac{-1}{\sqrt{2}}$	$\dfrac{+1}{\sqrt{2}}$	0
z′	---	---	---

(b) Given that $S_{11} = 0.98 \times 10^{-11}$/Pa, $S_{12} = -0.27 \times 10^{-11}$/Pa, and $S_{44} = 1.5 \times 10^{-11}$/Pa, find S'_{1111} which is $1/E'$ in the [110].

Remember that there are 21 terms possible on the right-hand side of the equation, although many may have coefficients equal to zero.

B.2.10 Given below are the room-temperature compliances of several refractory metals. All of these metals have BCC crystal structures.

(a) Which of these metals has the highest stiffness along the direction of closest spacing of atoms?

(b) Give the elastic strain expected in the [100] for a Cr crystal compressed by a stress in the [001] of 5 MPa.

(c) If the Cr crystal in part (b) has a square cross section with {001} faces before loading, will it still be square while the compression is applied?

B.2.11 The final equation given in Example 2.4 provides the variation of S'_{33} with orientation (Φ) for axisymmetric composites and hexagonal crystals. Using this equation, plot Young's modulus surfaces for cadmium and titanium single crystals (Table 2.8). Plot the surfaces on the same axes to make a comparison.

B.2.12 Which of the cubic metals in Table 2.8 is most isotropic? Least isotropic?

C.2.1 A cylindrical drawn polymer fiber is reported to have elastic constants (in GPa) of $C_{11} = C_{22} = 0.5$, $C_{33} = 18$, $C_{12} = 1$, $C_{13} = C_{23} = 3$, and $C_{44} = C_{55} = 0.8$. Find C' for a rotation of $\Phi = 30°$. Compare this result with C' for $\phi 1 = 30°$ and $\Phi = 30°$. (Note the axisymmetry.)

C.2.2 Find S_{11}', S_{14}', and S_{44}' for each the rotation in B.2.8.

C.2.3 For a tensile test on a cylindrical specimen that is deformed by a stress in the z (or 3-direction), what will be Poisson's ratios? (Write your answer in terms of strains e_{ij}, but with specific choices of i and j.)

C.2.4 A silica glass has Young's modulus of 80 GPa and a shear modulus of 31.5 GPa. We plan to reinforce this glass with 20 v/o particulates of tungsten carbide (WC), which has Young's modulus of 530 GPa and a shear modulus of 219 GPa. Compare the expected composite Young's moduli versus volume fraction for both upper and lower bound estimates assuming that each phase is isotropic.

Refractory metal	Group on periodic chart	Anisotropy factor	S_{11}	S_{12}	$S_{44}(10^{-11}$/Pa)
V	VB	0.78	0.68	−0.23	2.35
Nb	VB	0.51	0.66	−0.23	3.48
Ta	VB	1.56	0.69	−0.16	1.21
Cr	VIB	0.69	0.30	−0.04	0.99
Mo	VIB	0.78	0.28	−0.08	0.91
W	VIB	1.0	0.24	−0.07	0.62

C.2.5 (a) For the properties given in Problem C.2.4, write the compliance matrix as S_{ij} for 100% glass and 100% WC.

(b) Calculate the corresponding effective compliance for an equal fraction composite, $\langle S_{ijkl}\rangle^{Reuss}$

(c) Calculate the corresponding effective stiffnesses, $\langle C_{ijkl}\rangle^{Reuss}$ $\leftarrow$ Voigt

(d) To find the $\langle C_{ijkl}\rangle^{Voigt}$ (Reuss) for an equal fraction composite, find the S_{ij} matrix for 100% glass and 100% WC and calculate the effective stiffnesses.

(e) Discuss the values found for $\langle C_{ijkl}\rangle^{Voigt}$ and $\langle C_{ijkl}\rangle^{Reuss}$.

C.2.6 Find the principal stresses for the stress tensor

$$\sigma = \begin{vmatrix} 10 & 12 & -5 \\ 12 & 4 & 3 \\ -5 & 3 & -5 \end{vmatrix} MPa$$

C.2.7 Describe the shape of the three-dimensional Young's modulus surface for cubic materials with anisotropy $A \ll 1$ and make a sketch.

C.2.8 Find the compliance values for the polymer fiber in Problem C.2.1. What is Young's modulus along the fiber axis?

C.2.9 Estimate the stiffness properties of an aluminum alloy single crystal containing 50 percent cuboidal silicon particles by weight, assuming that the cubic unit cells of both materials are aligned with one another. Find the Voigt prediction and the Reuss prediction.

In channel die compression, the material is deformed in plane strain by placing the cube in a rectangular slot that fits snuggly against two sides. The cube is free to deform in the other direction as it is compressed from the normal direction. The deformation is analogous to that in rolling with compressive deformation in the normal direction (ND), extension in the free direction or rolling direction (RD), and near-zero deformation in the confined direction or transverse direction (TD). To reach the final dimensions, the plastic deformation in this first step is given in true strain as

$$\varepsilon^{(1)} = \begin{vmatrix} \ln\dfrac{\sqrt{8}}{2} & 0 & 0 \\ 0 & 0 & 0 \\ 0 & 0 & \ln\dfrac{\sqrt{2}}{2} \end{vmatrix} = \begin{vmatrix} 0.347 & 0 & 0 \\ 0 & 0 & 0 \\ 0 & 0 & -0.347 \end{vmatrix}$$

where $\sqrt{8}$ cm is the x-dimension, the y-dimension is unchanged at 2 cm, and the width of the die, $\sqrt{2}$ cm, is the z-dimension after the first deformation step.

In the second deformation step, the x-dimension is held at $\sqrt{8}$ cm and the material is free to deform in the y-direction as it is again in the z-direction. This time the deformation is

$$\varepsilon^{(2)} = \begin{vmatrix} 0 & 0 & 0 \\ 0 & \ln\dfrac{\sqrt{8}}{2} & 0 \\ 0 & 0 & \ln\dfrac{\sqrt{2}}{2} \end{vmatrix} = \begin{vmatrix} 0 & 0 & 0 \\ 0 & 0.347 & 0 \\ 0 & 0 & -0.347 \end{vmatrix}$$

Assume that the stress applied to produce this deformation was $s = 100$ MPa. Using the flow rules for the first deformation step, the strain ratios are

$$0.347{:}0{:}-0.347$$

Applying the flow rules given in Eq. 3.24, if the magnitude of the stress in the confining direction is one-half that of the deformation stress, the deformation will proceed with equal and opposite strains in the x- and z-directions, respectively. This stress level can be used in both the von Mises and Tresca criteria to predict deformation under other conditions. Using the von Mises criterion from Eq. 3.4,

$$\left(0-\frac{1}{2}s\right)^2 + (s-0)^2 + \left(s-\frac{1}{2}s\right)^2 = C_{von\ Mises}$$

$$\frac{3}{2}s^2 = 15{,}000(\text{MPa})^2$$

This fixes the yield criterion at one point. Because the yield criterion is simply an infinite cylinder, it also fixes all other values. The yield stress Y for simple compression predicted by the von Mises stress is then

$$(0-0)^2 + (Y-0)^2 + (Y-0)^2 = 15{,}000 \ (\text{MPa})^2$$

so we can solve for the yield stress as follows:

$$Y = \sqrt{\frac{15{,}000}{2}} = 86.6 \text{ MPa}$$

Consequently, the von Mises criterion predicts that the applied stresses for the simple compression will be less than for the channel die compression by

$$Y = \left(\sqrt{3}/2\right)s$$

Using the Tresca criterion,

$$s - 0 = C_{Tresca}$$

the nature of the shape change that may have occurred so as to help understand any repairs that might be necessary.

First, we will need to determine the principal stresses as shown in Chapter 2. We know that $\sigma_{33} = 120$ MPa is already a principal stress. We can find the other two principal stresses using Eq. 2.14:

$$\frac{120+240}{2} \pm \sqrt{\left(\frac{120-240}{2}\right)^2 + (80)^2} = 280 \text{ and } 80 \text{ MPa}$$

Then, if we use the von Mises criterion, we can write

$$\sqrt{\frac{(80-280)^2 + (80-(-120))^2 + (280-(-120))^2}{2}} = 346 \text{ MPa}$$

which is clearly greater than the specified yield stress. To estimate the amount of deformation that occurred locally, we first assume that hardening is isotropic. If we do so, we can use Eq. 3.19 to roughly estimate the amount of effective shear strain. Using the given values, we can calculate

Effective strain	Effective stress (MPa)
0.002	250
0.005	286
0.01	318
0.015	338
0.02	353
0.025	365

The values above suggest that the total amount of deformation expected is about 2 percent effective strain. If we want to predict the shape change, we can use the Levy–von Mises relations of Eq. 3.23 and 3.24.

Using these relations yields the following principal strains.

$$\varepsilon_1 = \frac{0.02}{346}\left[280 - \frac{1}{2}(80+(-120))\right] = 0.017$$

$$\varepsilon_2 = \frac{0.02}{346}\left[80 - \frac{1}{2}(280+(-120))\right] = 0.00$$

$$\varepsilon_3 = \frac{0.02}{346}\left[-120 - \frac{1}{2}(280+80)\right] = -0.017$$

We can check our answer to see that the strains sum to zero, as they should for plastic deformation.

Whenever deformation is driven by a given stress state that meets a criterion for shear deformation, we can express this in a single term called the effective shear stress. Related to this effective shear stress is a single term that we can also use to represent the amount of shear deformation taking place. Both of these terms are used to describe deformation in Chapter 8. Using the values from this example, the effective shear stress is

$$\tau_{\text{eff}} = \sqrt{\frac{(80-280)^2 + (80-(-120))^2 + (280-(-120))^2}{6}} = 200 \text{ MPa}$$

and the effective shear strain is

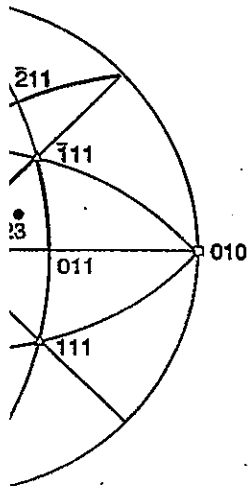$$\gamma_{\text{eff}} = \sqrt{2\left(0.017^2 + (-0)^2 + (-0.017)^2\right)} = 0.024$$

∎

ms

leformation on crys-
s. The Appendix to
square-cross-section
p direction [$\bar{1}01$] for
planes and directions
ward the tensile axis.
g machine. The rota-
allel to the tensile or
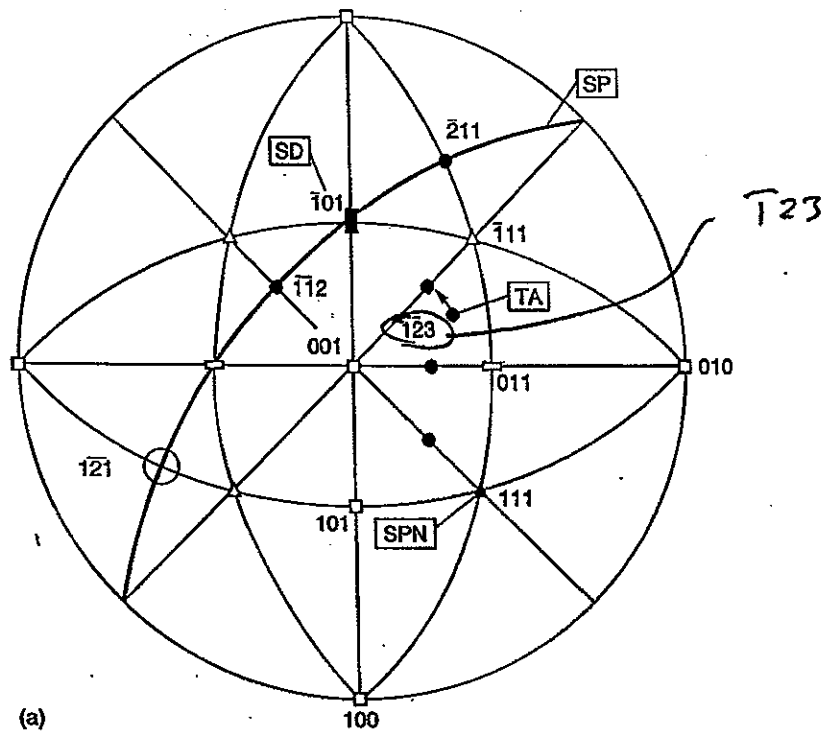le stereographic pro-
axis should rotate as
unterclockwise rota-

ird stereographic tri-
any triangle because
hown on the triangle
imetry have the same
cur on particular slip
: detail in Chapter 4).
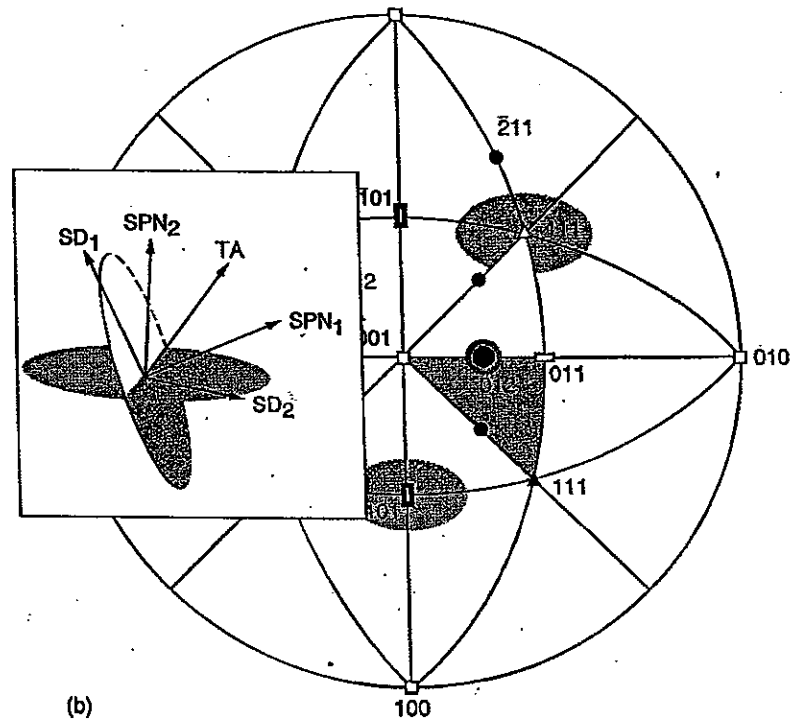$_{crss}$. For FCC metals,
l planes, {111}, pro-

isile axis in the stan-
is for one of the three
lich is the easiest slip

and slip plane normal
aphic projection.

FIG. 3.15 (a) Rotation of the tensile axis during testing of a cubic crystal oriented for single slip relative to the crystal axis. In compression, the rotation would have the opposite sense. The rotation related to simple shear occurs about the [$1\bar{2}1$]. (b) Slip on two equivalent slip systems at the boundary of the standard stereographic triangle.
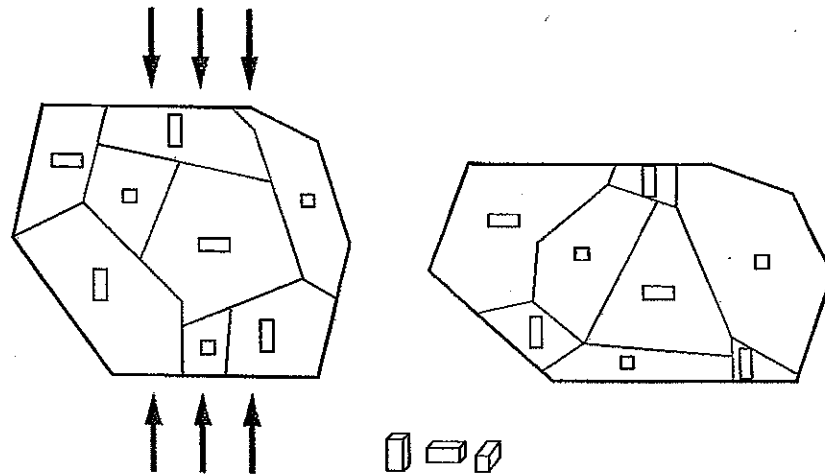
FIG. 3.18   Compression of a tetragonal crystal containing domains. All three possibilities for the domains are shown in projection within the grain.

low, because large strains would involve high resistances to boundary motion. In materials that do not otherwise deform by slip, such deformation mechanisms can enable these materials to be more resistant to crack propagation.

3.2.4   Deformation of Polycrystalline Materials

Polycrystalline materials consist of crystallite aggregates differing in orientation. If a polycrystalline material is considered to consist of randomly oriented grains, then all properties, including plasticity, should be nondirectional or isotropic (see Hosford, 1993).[1] To evaluate the problem of a polycrystal, Sachs considered that if the problem is treated for the average value of the Schmid factor, for randomly oriented crystals the value of slip in an FCC metal would be 2.238, so that $\sigma = 2.238\tau$. Taylor noted that by allowing single slip within each grain, Sachs' model would not allow the grains to deform while maintaining intact grain boundaries. Taylor developed a new model that required that slip take place with the grains deforming uniformly and thereby maintaining all boundaries. Because each grain in the material would then undergo the same strains as those imposed externally on a macroscopic basis, five independent terms of the nine in a plastic strain tensor must be identical ($\varepsilon_{12} = \varepsilon_{21}$, $\varepsilon_{13} = \varepsilon_{31}$, $\varepsilon_{23} = \varepsilon_{32}$, and $\varepsilon_{11} + \varepsilon_{22} + \varepsilon_{33} = 0$).

Taylor's analysis of slip was based on the increment of work per unit volume, dw, that is produced by slip on all participating slip systems inside one grain as

$$dw = \sum_i \tau_i |d\gamma_i| \qquad (3.30)$$

where τ_i is the magnitude of shear stress required for slip on slip system i. The term $|d\gamma_i|$ is the absolute value of the slip increment on the same slip system. For a single type of slip system—e.g., <110> {111} in FCC metals—the magnitude of shear stress required to produce deformation is initially equal for all specific slip systems of this type at the start of deformation. As deformation proceeds, the work hardening on one slip system may proceed at a different rate than on other slip systems. Also, in materials with multiple <uvw>{hkl} possibilities for slip systems, the differences in the shear stress required for deformation and

[1]A good rule of thumb for deformation studies is that the stress is applied over a cross section containing at least 10 grains.

$$\frac{\Delta V}{V} = \int f(g)dg \tag{3.33}$$

where $\Delta V/V$ is the volume of grains under consideration and $f(g)$ is a function describing grain orientations. The ODF is commonly normalized such that a random sample would have an ODF of 1 at all points. If the magnitude of a point within a contour in Fig. 3.19a is greater than 1, that orientation relationship occurs more frequently than it would in a random sample. If the magnitude is less than 1, that orientation relationship is depleted when compared with the frequency of its occurrence in a random sample. A single crystal represents an infinite degree of preferred orientation. Preferred orientations that result from processing history in materials can be advantageous or deleterious depending on the final application of the material. Preferred orientations in rolled steels are often designed to fulfill specifications for formability in later shaping operations. In aluminum alloys, the plastic anisotropy of the rolled sheet hinders the efficiency of the deep drawing process for manufacture of aluminum beverage cans, as demonstrated in Fig. 3.20.

The texture of metals from rolling is expressed in terms of the rolling direction <uvw> and the plane of the rolled sheet {hkl} (see Fig. 2.9). For extruded materials, the expected textures give pole figures that are axisymmetric about the extrusion axis, as shown in Fig. 3.19c. The schematic 111 and 110 pole figures both correspond to a cubic material with a <111> extrusion direction. The 111 pole figure shows a large number of orientations in the extrusion direction (top and bottom). The two symmetric bands also shown on the 111 pole figure represent the positions of the three <111> that lie approximately 70° from the <111> that lie concentrated in the extrusion direction. Typical textures in engineering alloys expressed in this way are given in Table 3.4.

TABLE 3.4 Typical Textures for Various Ductile Metals

Material	Rolling Rolling texture
	<RD> {RP}
FCC metals, Ag, brass, stainless steel	<$\bar{1}$12> {110}, <001> {110}
FCC metals, Cu, Ni, Al	<11$\bar{1}$> {112}, <112> {$\bar{4}$21}
BCC metals	<110> {001}, <1$\bar{1}$0> {111},
	<112> {111}
HCP metals, Ti, Zr	[10$\bar{1}$0] {0001} tilted $\approx$ 30° from plane
HCP metals, Mg	[11$\bar{2}$0] {0001}

Material	Extrusion Extrusion direction
FCC metals, Ag, brass	Strong <100>, weak <111>
FCC metals, Cu, Au, Ni, Al	Strong <111>, weak <100>
BCC metals	Strong <110>
HCP metals	Strong <hk0>

Material	Axisymmetric Compression Compression direction
FCC metals	<110> strong
BCC metals	Strong <111>, weak <100>
HCP metals	Strong [0001]

A.3.2 Calculate the effective strain for part (c) of Problem A.3.1. For a 1-cm^3 cube, what would be the equivalent degree of deformation in simple compression?

A.3.3 Plot the Tresca criterion for a tensile yield stress of 5 MPa, defining each of the lines or facets of the yield surface by a separate equation.

A.3.4 Plot the von Mises criterion for a yield stress of 5 MPa.

A.3.5 An individual crystal is deformed such that slip planes 1 μm apart are displaced by 0.1 μm. What is the glide strain? If both θ and λ are 45°, what is the axial strain?

A.3.6 Write the general tensor expression of the type shown in Eq. 3.44 for transformation between the following crystal structures.

(a) Cubic to tetragonal

(b) Tetragonal to orthorhombic

(c) Orthorhombic to monoclinic

(d) Monoclinic to triclinic

B.3.1 Plot a projection of the Tresca criterion onto an s_1–s_3 section of the yield surface at a hydrostatic pressure of 10 MPa for a tensile yield stress of 5 MPa.

B.3.2 Repeat Problem B.3.1 for the von Mises criterion.

B.3.3 For the following stress states (in MPa), determine if the Tresca or von Mises criterion has been exceeded, assuming a tensile yield stress of 10 MPa.

(a) $\begin{vmatrix} 0 & 0 & 4 \\ 0 & 8 & 0 \\ 4 & 0 & 0 \end{vmatrix}$

(c) $\begin{vmatrix} 10 & -2 & 0 \\ -2 & 5 & 0 \\ 0 & 0 & 3 \end{vmatrix}$

(b) $\begin{vmatrix} 0 & 0 & 0 \\ 0 & 10 & 12 \\ 0 & 12 & -10 \end{vmatrix}$

(d) $\begin{vmatrix} 12 & 0 & 1 \\ 0 & 0 & 0 \\ 1 & 0 & 3 \end{vmatrix}$

B.3.4 Calculate the resolved shear stress for slip on SP = (100) and the SD = [0$\bar{1}$1] for a stress of 10 MPa applied along the stress axes.

(a) [100]

(d) [123]

(b) [110]

(e) [2$\bar{1}$1]

(c) [$\bar{1}$23]

(f) [$\bar{1}$21]

B.3.5 Calculate the axial strain ε along [$\bar{1}$23] for a glide shear strain of γ = 0.05 on the following proposed slip systems for a cubic material (make sure the combinations give valid slip systems).

(a) [110] ($\bar{1}$01)

(e) [111] (0$\bar{1}$1)

(b) [111] ($\bar{1}$01)

(f) [111] ($\bar{1}\bar{1}$2)

(c) [$\bar{1}$01] (111)

(g) [110] ($\bar{1}\bar{1}$2)

(d) [111] ($\bar{1}$10)

(h) [101] ($\bar{1}\bar{1}$1)

B.3.6 Which of the following are likely slip systems in a tetragonal material with $c/a = 2$?

(a) [110] (001)

(d) [10$\bar{1}$] (101)

(b) [100] (011)

(e) [111] ($\bar{1}$01)

(c) [1$\bar{1}$0] (110)

(f) [$\bar{1}$01] (111)

B.3.7 Find and sketch in an s_1 – s_3 section of the von Mises yield surface the value of the plastic strain ratio for the following stress states (in MPa). Assume that only yielding takes place in each case, and also calculate the value of Y.

(a) $\begin{vmatrix} 0 & 0 & 4 \\ 0 & 8 & 0 \\ 4 & 0 & 0 \end{vmatrix}$

(c) $\begin{vmatrix} 12 & 0 & 1 \\ 0 & 0 & 0 \\ 1 & 0 & 3 \end{vmatrix}$

(b) $\begin{vmatrix} 0 & 0 & 0 \\ 0 & 10 & 12 \\ 0 & 12 & -10 \end{vmatrix}$

(d) $\begin{vmatrix} 10 & -2 & 0 \\ -2 & 5 & 0 \\ 0 & 0 & 3 \end{vmatrix}$

B.3.8 Plot the Schmid factor for a set of FCC crystals lying at each of the boundaries of the standard stereographic triangle (pick at least eight for each boundary, including the symmetric points at the corners).

B.3.9 Determine how the factor of 3η comes into being if we consider that Eq. 3.41 relies on an assumption that the von Mises criterion holds. How would this equation change if the Tresca criterion were assumed?

B.3.10 Chen and Reyes-Morel (1986) were able to deform a tetragonal zirconia polycrystal (TZP) in compression. Explain which features of the transformation strain tensor (Eq. 3.44) would be required to make deformation in compression possible.

B.3.11 (a) A BCC crystal with a [$\bar{1}$23] orientation undergoes single slip on a ($\bar{1}\bar{1}$2) plane. Find the slip direction that is most likely.

(b) Sketch a standard stereographic triangle, showing clearly the direction of rotation of the stress axis for compression.

B.3.12 Write the physically distinct slip systems for slip in BCC metals on the slip system <1$\bar{1}$1> {21$\bar{1}$}.

B.3.13 Write the physically distinct slip systems for slip on both types of slip systems given for rock salt materials in Table 3.1.

B.3.14 Find the number of slip systems in Table 3.2 that have the same Schmid factor for the following positions on a standard stereographic triangle: (a) the [001]–[011] boundary; (b) the [011]–[$\bar{1}$11] boundary; (c) the [001]–[$\bar{1}$11] boundary.

B.3.15 For a material with Young's modulus of 100 GPa, a yield strength of 50 MPa, and parabolic work hardening behavior, write the stress for a strain of 2%.

For this material, work hardening occurs at $s_{plastic} = 50\sqrt{\varepsilon}$ MPa.

C.3.1 Find the simplified expression relating the effective shear stress and the following stress states in terms of σ.

(a) $\begin{vmatrix} \sigma & 0 & 0 \\ 0 & 0 & 0 \\ 0 & 0 & 0 \end{vmatrix}$

(b) $\begin{vmatrix} \sigma & 0 & 0 \\ 0 & \sigma & 0 \\ 0 & 0 & 0 \end{vmatrix}$

(c) $\begin{vmatrix} 2\sigma & 0 & 0 \\ 0 & 0 & 0 \\ 0 & 0 & 0 \end{vmatrix}$

(d) $\begin{vmatrix} 0 & \sigma & 0 \\ \sigma & 0 & 0 \\ 0 & 0 & 0 \end{vmatrix}$

(e) $\begin{vmatrix} \sigma & 0 & 0 \\ 0 & 0 & 0 \\ 0 & 0 & -\sigma \end{vmatrix}$

(f) $\begin{vmatrix} \sigma & \sigma & 0 \\ \sigma & \sigma & 0 \\ 0 & 0 & 0 \end{vmatrix}$

C.3.2 Calculate the Schmid factor of the dominant slip system for a cubic crystal pulled in a direction with cosines of [0.81 −0.46 0.36], assuming <111> {110} slip.

(a) Write the Euler rotations ($\phi1$, Φ, $\phi2$) required to reach this orientation.

(b) Write the integer direction indices for a direction that lies within 5°.

(c) Show this tensile direction and highlight the cube triangle on a stereographic projection.

(d) Give the specific easiest slip system and the Schmid-factor value.

(e) Assuming that slip occurs only as a simple shear rotation on the slip system, what angle of rotation would take place before a second slip system would have an equivalent resolved shear stress? Which slip system(s) would that be?

C.3.3 Repeat Problem C.3.2 using <110> {111} slip.

C.3.4 Repeat Problem C.3.3 using <110> {110} slip.

C.3.5 Consider the Rankine criterion, wherein yielding is predicted if any principal stress exceeds Y (see Fig. 3.5). Does this criterion fulfill the conditions for shear deformation given at the beginning of this chapter? Sketch the yield surface in three dimensions and with an $s_2 = 0$ section.

C.3.6 From a macroscopic viewpoint, hot pressing, which combines deformation with sintering to produce densification, is a deformation process. Describe the type of yield surface you would expect for hot pressing, including the case for isostatic pressure. Sketch both a three-dimensional section and an $s_2 = 0$ section of the yield surface.

C.3.7 Consider the yield condition for transformable zirconia materials in tension and compression. Perform a calculation to find the crystal orientation wherein the transformation should be easiest for each case. (*Hint:* using the resolved tensor components, relate the stresses and strains such that the most work is produced for a given applied stress.)

C.3.8 Derive Eq. 3.15.

C.3.9 Find that the necking strain is twice the strain hardening exponent, n, for balanced biaxial tension.

C.3.10 Discuss the implications of Fig. 3.8 on the value of the anisotropy factor R.

C.3.11 Find ε and ω relative to a unit cube using Eq. 3.27 and 3.29 for slip on $[\bar{1}10]$ (111).

C.3.12 The actual transformation from γ to α iron involves a change in the defined crystal axes. Describe this change in the coordinate system by a Euler angle rotation. Is Eq. 3.44 defined in terms of the original γ axes or in terms of the axes for FCC iron or martensite?
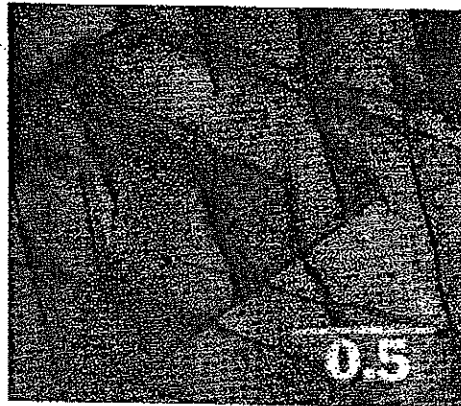
FIG. 4.3 Transmission electron micrograph of straight <111> screw dislocations in tungsten following plastic deformation (by K. J. Bowman and R. Gibala, unpublished). Three sets of long <111> screw dislocations are shown. The fourth set lies nearly perpendicular to the thin foil of material. The other markings and contrast are mostly surface relief and strain fields in the TEM foil (marker is in microns).

As evaluation of deformation processes has progressed, the influences of the presence or absence of dislocations in the deformation and fracture of materials has become a topic of great importance. Single crystals made from materials that are normally readily deformed become extremely resistant to plastic deformation if they are made with very few dislocations. To define the quantity of dislocations within a material, the dislocation density $\rho_\perp$ is given as

$$\rho_\perp = \frac{L_\perp}{V} \approx \frac{\#_\perp}{A} \tag{4.2}$$

where $L_\perp$ is the total length (m) of the dislocations within a given volume V (m^3), $\#_\perp$ is the number of dislocations, and A is the area. An approximation of dislocation density that also fits these units is dislocation number per unit area. When dislocation densities are determined from micrographs such as those shown in Fig. 4.3 and 4.4, edge effects often cause
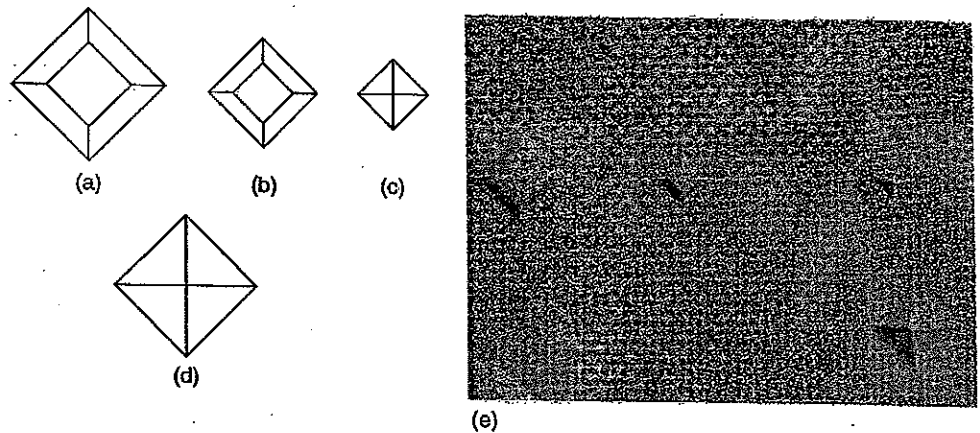

(a) (b) (c)

(d)

(e)

FIG. 4.4 Schematic showing motion of a dislocation as tracked by repeated etching of lithium fluoride (LiF) crystals. (a) The largest smooth bottom etch pit was formed during the first etching treatment. (b) The medium smooth bottom etch pit was formed after dislocation motion and the second etch treatment. (c) The third sharp bottom etch (indicating the final dislocation position) was formed after additional dislocation motion and the third etch treatment. (d) The large sharp bottom pit shows dislocations that did not move from the applied stresses. Part (e) shows the actual images of the dislocation etch pits. (Gilman and Johnston, 1957, used with permission)

where the width of the lower right pit is about 20μm

$$\sigma_{22} = \frac{\mu b}{2\pi(1-v)} \frac{y(x^2-y^2)}{(x^2+y^2)^2} \qquad (4.3b)$$

$$\sigma_{12} = \sigma_{21} = \frac{\mu b}{2\pi(1-v)} \frac{x(x^2-y^2)}{(x^2+y^2)^2} \qquad (4.3c)$$

where b is the magnitude of the Burgers vector. Because for particular positions the expressions above include normal stresses, there must also be a Poisson effect given by Hooke's law such that $\sigma_{33} = -v(\sigma_{11} + \sigma_{22})$. Figure 4.9 shows the relative magnitude of σ_{11} and the mean or hydrostatic stress as the dislocation core is approached.

At small distances from the core of the dislocation, the magnitudes of the stresses become quite large owing to large strains. Since the strains are large near the dislocation core, deviations from linear elasticity prevent the possibility of "infinite" stresses at the singularity.

EXAMPLE 4.2   *Stresses Near Edge Dislocation Cores*

Using the values for an aluminum alloy, we will calculate the magnitudes of the stresses σ_{11} given by Eq. 4.3a for positions along the y-axis, which means that the x-value is zero.

$$\mu = 25 \text{ GPa} \qquad v = 0.35 \qquad b = 2.9 \times 10^{-10} \text{ m}$$

$$\sigma_{11} = \frac{-\mu b}{2\pi(1-v)} \frac{y^3}{y^4} = \frac{-25 \text{ GPa}(2.9\times 10^{-10} \text{ m})}{2(3.14)(1-0.35)} \left(\frac{1}{y}\right) = \frac{-1.8 \times 10^{-9} \text{ GPa·m}}{y}$$

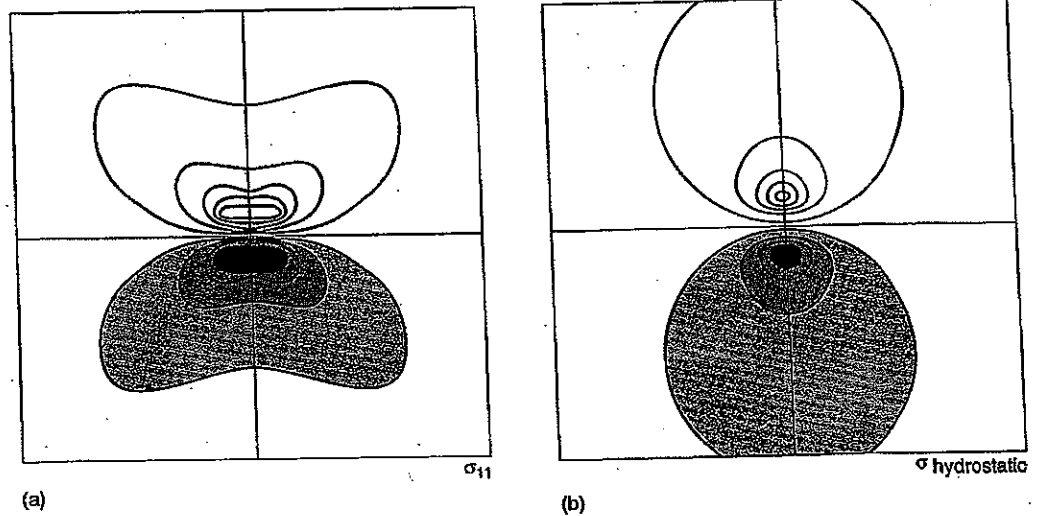(a)   (b)

FIG. 4.9   Gray scale plots of the stresses (a) σ_{11} and (b) hydrostatic stress $= (\sigma_{11} + \sigma_{22} + \sigma_{33})/3$ from Eq. 4.3 as a function of position around the centered edge dislocation core from Fig. 4.7. The extra half-plane lies in the top half of each figure. White represents compressive stress, and gray represents tensile stress.

Distance (10^{-10} m)	Stress (GPa)
40	−0.4
30	−0.6
20	−0.9
10	−1.8
0	∞
−10	1.8
−20	0.9
−30	0.6
−40	0.4

As shown in the calculation results, the magnitudes of the stresses become quite large, with this linear elastic relation predicting infinite stresses at the dislocation core, large tensile stresses just below the glide plane, and large compressive stresses just above the glide plane. At the large strains near the dislocation core, an assumption of linear elasticity is not a good one. ∎

The elastic distortion of the material outside the dislocation core (wherein the elastic calculation would give an infinite result) can be calculated as a function of distance from the dislocation using

$$E_{elastic} = \frac{\mu b^2 \ell}{4\pi(1-v)} \int_{r_o}^{R} \frac{dx}{x}$$

$$= \frac{\mu b^2 \ell}{4\pi(1-v)} \ln \frac{R}{r_o}$$

(4.4)

The core radius r_0 and the outer radius R can then be used to calculate the energy of the dislocation, and ℓ is the dislocation length. The magnitude of r_0 should be chosen such that the deformation is still small enough to be considered elastic. The magnitude of the outer radius can extend to the crystal surfaces if only one dislocation is present in the crystal. For crystals containing many dislocations, half the spacing between dislocations is often employed to provide an estimate of the elastic energy surrounding each dislocation. Equation 4.4 also shows that the energy of the dislocation is linearly dependent on the shear modulus and the dislocation length. The dislocation energy has a squared dependence on the magnitude of the Burgers vector.

The plane of slip for an edge dislocation is completely determined by the plane defined by the Burgers vector and line direction. With reference to Chapter 3, it is then clear that the cross product of the slip plane normal, SPN, and the Burgers vector gives the line direction for the edge dislocation.

EXAMPLE 4.3 *The Elastic Energy of Edge Dislocation*

We can calculate the energy of an edge dislocation using Eq. 4.4. Consider 1 cm^3 of a cold-worked material with $\mu = 50$ GPa, $b = 2.5 \times 10^{-10}$, and $v = 0.3$. We will use a cutoff of $4b = 1 \times 10^{-9}$ m for the magnitude of r_0. With a dislocation density of $\rho_{\perp} = 1 \times 10^{14}$ m^{-2}, we can estimate an average spacing of $L = (1 \times 10^{14})^{-0.5} = 1 \times 10^{-7}$ m. The outer radius can then be set to half this value, $R = 5 \times 10^{-8}$ m. The total length of dislocation in our 1 cm^3 of material is $l = (1 \times 10^{-6}$ m$^3)(10^{14}$ m/m$^3) = 1 \times 10^8$ m. Then the elastic energy is calculated as

$$E_{elastic} = \frac{\left(50 \times 10^9 \text{ N/m}^2\right)\left(2.5 \times 10^{-10} \text{ m}\right)^2 \left(1 \times 10^8 \text{ m}\right)}{4\pi(1-0.3)} \ln\left(\frac{5 \times 10^{-8} \text{ m}}{1 \times 10^{-9} \text{ m}}\right) = 0.14 \text{ Nm} \quad ∎$$

1×10^{-9} m

Distance (10^{-10} m)	Stress (GPa)
40	−0.4
30	−0.6
20	−0.9
10	−1.8
0	∞
−10	1.8
−20	0.9
−30	0.6
−40	0.4

As shown in the calculation results, the magnitudes of the stresses become quite large, with this linear elastic relation predicting infinite stresses at the dislocation core, large tensile stresses just below the glide plane, and large compressive stresses just above the glide plane. At the large strains near the dislocation core, an assumption of linear elasticity is not a good one. ∎

The elastic distortion of the material outside the dislocation core (wherein the elastic calculation would give an infinite result) can be calculated as a function of distance from the dislocation using

$$E_{elastic} = \frac{\mu b^2 \ell}{4\pi(1-v)} \int_{r_0}^{R} \frac{dx}{x}$$

$$= \frac{\mu b^2 \ell}{4\pi(1-v)} \ln \frac{R}{r_0}$$

(4.4)

The core radius r_0 and the outer radius R can then be used to calculate the energy of the dislocation, and ℓ is the dislocation length. The magnitude of r_0 should be chosen such that the deformation is still small enough to be considered elastic. The magnitude of the outer radius can extend to the crystal surfaces if only one dislocation is present in the crystal. For crystals containing many dislocations, half the spacing between dislocations is often employed to provide an estimate of the elastic energy surrounding each dislocation. Equation 4.4 also shows that the energy of the dislocation is linearly dependent on the shear modulus and the dislocation length. The dislocation energy has a squared dependence on the magnitude of the Burgers vector.

The plane of slip for an edge dislocation is completely determined by the plane defined by the Burgers vector and line direction. With reference to Chapter 3, it is then clear that the cross product of the slip plane normal, SPN, and the Burgers vector gives the line direction for the edge dislocation.

EXAMPLE 4.3 *The Elastic Energy of Edge Dislocation*

We can calculate the energy of an edge dislocation using Eq. 4.4. Consider 1 cm³ of a cold-worked material with $\mu = 50$ GPa, $b = 2.5 \times 10^{-10}$, and $v = 0.3$. We will use a cutoff of $4b = 1 \times 10^{-9}$ m for the magnitude of r_0. With a dislocation density of $\rho_\perp = 1 \times 10^{14}$ m^{-2}, we can estimate an average spacing of $L = (1 \times 10^{14})^{-0.5} = 1 \times 10^{-7}$ m. The outer radius can then be set to half this value, $R = 5 \times 10^{-8}$ m. The total length of dislocation in our 1 cm³ of material is $l = (1 \times 10^{-6}$ m³$)(10^{14}$ m/m³$) = 1 \times 10^{8}$ m. Then the elastic energy is calculated as

$$E_{elastic} = \frac{\left(50\times10^9 \ N/m^2\right)\left(2.5\times10^{-10} \ m\right)^2\left(1\times10^8 \ m\right)}{4\pi(1-0.3)} \ln\left(\frac{5\times10^{-8} \ m}{1\times10^{-8} \ m}\right) = 0.14 \ Nm$$

space

∎

JOHANNES MARTINUS BURGERS (1895–1981)

This specialist in fluid mechanics was appointed as professor at the Technical University of Delft (Netherlands) at the age of 23. He is credited with the first real description of a screw dislocation in 1939. He also helped establish early forms of the expressions for dislocation displacements and dislocations in subgrain boundaries.

4.2.2 Screw Dislocations

A screw dislocation is a spiral defect within a material. The nature of the screw dislocation is similar to a simple parking garage wherein one circuit translates you and your auto up or down one level. Etching of surfaces intersected by screw dislocations can show the spiral character of the screw dislocation (see Fig. 4.10). For consideration of a screw dislocation in a crystal, the relationship between the screw dislocation and an edge dislocation provides some insight, as shown in the three views of the same dislocation in Fig. 4.11. Of course, the most distinctive difference between edge and screw dislocations is the relationship between the line direction of the dislocation and the Burgers vector. For the edge dislocation, these vectors are orthogonal; in the case of screw dislocations, the Burgers vector and the line direction are either parallel or antiparallel. Screw dislocations with the same Burgers vector, but opposite line directions, have the opposite sign of the twist. Unlike the case of the edge dislocation, the screw dislocation does not define a single glide plane in which it can move, but it is possible for it to move on any plane that contains its Burgers vector if the shear stress required for motion on that plane is exceeded.   *rolled*

The distortion of a cylindrical element of material by a screw dislocation in the material is shown in Fig. 4.12a. The screw dislocation of the *rolled* element is equivalent to a simple shear of the unrolled cylindrical element, as shown in Fig. 4.12b. When translated back into the coordinate system of the dislocated cylinder, the only shear strains possible are those consisting of shear strains with z-components. These strains are given in cartesian and cylindrical coordinates as

$$\varepsilon_{13} = \varepsilon_{31} = \frac{-b}{4\pi} \frac{y}{\left(x^2 + y^2\right)} = \frac{-b}{4\pi} \frac{\sin\theta}{r} \qquad (4.5a)$$

$$\varepsilon_{23} = \varepsilon_{32} = \frac{b}{4\pi} \frac{x}{\left(x^2 + y^2\right)} = \frac{b}{4\pi} \frac{\cos\theta}{r} \qquad (4.5b)$$

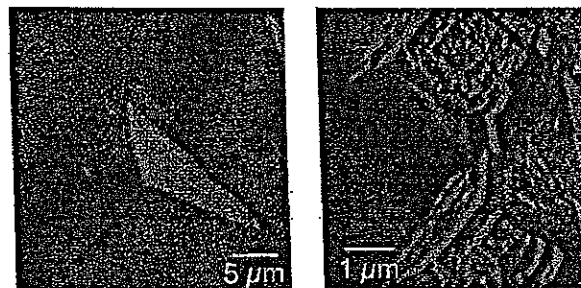**FIG. 4.10** Dislocation etch pits of <111> screw dislocations in tungsten (a BCC metal). (a) Pits for screw dislocations that lie nearly orthogonal to the surface. (b) Etch pits for dislocations at an angle to the surface, showing the spiral ledges associated with the screw dislocations (K. J. Bowman and R. Gibala, unpublished).

(a)   (b)

All other strains should be zero in an isotropic material. The associated stresses are given by

$$\sigma_{11} = \sigma_{22} = \sigma_{33} = \sigma_{12} = \sigma_{21} = 0 \qquad (4.6a)$$

$$\sigma_{13} = \sigma_{31} = \frac{-\mu b}{2\pi} \frac{y}{\left(x^2 + y^2\right)} = \frac{-\mu b}{2\pi} \frac{\sin\theta}{r} \qquad (4.6b)$$

$$\sigma_{23} = \sigma_{32} = \frac{\mu b}{2\pi} \frac{x}{\left(x^2 + y^2\right)} = \frac{\mu b}{2\pi} \frac{\cos\theta}{r} \qquad (4.6c)$$

FIG. 4.11 Screw dislocation viewed on a cube of material giving a screw dislocation connected to an edge dislocation to form a quarter loop. Top view is a three-dimensional view with an overhang of magnitude b on the front right portion of the crystal. Open arrows denote a shear stress that if high enough would cause expansion of the loop through motion of the edge dislocation to the back of the crystal and the screw dislocation to the left. Figure at lower left shows how the atoms in the top half of the crystal (solid black circles) are shifted forward from their positions above atoms in the lower half of the crystal (open gray circles). Schematic at lower right shows a perspective view of the quarter loop.

BIOGRAPHY

F. R. N. NABARRO (1916–   )

F. R. N. Nabarro is well known for developing physical formulations to describe the resistance to dislocation motion and mechanisms of diffusional creep. Nabarro has made many important contributions in elastic theory applied to dislocation.

Dislocations with widely distributed dislocation cores move more readily than dislocations with narrow cores. Dislocation width can be expressed in terms of the Burgers vector magnitude for a dislocation. The width of the edge dislocation can be defined as a fixed difference in displacement, Δu, of atoms above and below the slip plane. The width of the dislocation is then defined in terms of the distance over which the displacements are large enough so that linear elasticity theory does not apply. If, for example, we use bounds of $b/10$ for the strain level defining the extent of the dislocation's width, then the width of the dislocation core is much wider in Fig. 4.19a than in Fig. 4.19b. The plots of $|\Delta u|$ versus x show the disregistry (or deviation from perfect stacking) between the atoms above and below the plane.

The examples in Fig. 4.19 are expressed in terms of a stationary dislocation resting in its equilibrium, lowest-energy position. When a shear stress interacts with one of these dislocations, it imparts changes in the disregistry curves that change the energy of the dislocation. Peierls and Nabarro related the dislocation energy to the dislocation position by what is called the Peierls–Nabarro energy, E_{PN}

$$E_{PN} = \frac{\mu b^2 \ell}{\pi(1-v)} \exp\left(\frac{-2\pi w}{b}\right) \tag{4.12}$$

From this we can obtain the force or, even better, the stress required to move a dislocation by finding the maximum slope of E_{PN}. This is called the Peierls–Nabarro stress, τ_{PN}

$$\tau_{PN} = \frac{2\pi}{b^2} E_{PN} = \frac{2\mu\ell}{(1-v)} \exp\left(\frac{-2\pi w}{b}\right) \tag{4.13}$$

The magnitude of τ_{PN} is several orders of magnitude lower than predictions based on the theoretical shear strength and is often close to the observed critical shear stress values for deformation.

As expected, the Peierls–Nabarro model predicts slip between the planes with the widest separations. Extended, broad planar dislocation cores are found in materials with low τ_{CRSS}. The advantages of broad planar disregistry are one reason that edge dislocations are often more mobile than screw dislocations. For FCC and HCP metals, large dislocation
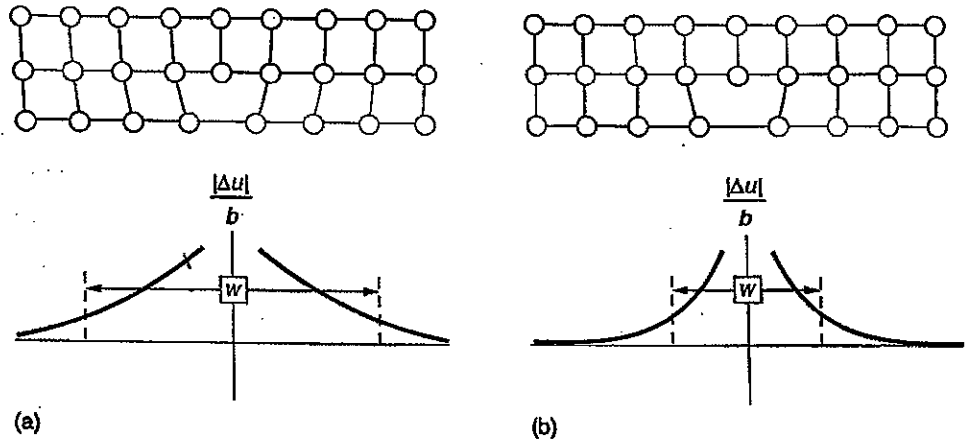

(a)   (b)

FIG. 4.19 (a) Edge dislocations with (a) wide and (b) narrow dislocation cores (after Hull and Bacon, 1984), with diagrams below showing the absolute value of the displacement $|\Delta u|$ from equilibrium in fractions of the Burgers vector magnitude b.

EGON OROWAN (1902–1989)

Egon Orowan was one of the founders of dislocation theory. As an undergraduate, he was inspired to think of dislocations from the deformation of zinc single crystals. Orowan also described expressions for strain from dislocation motion and mechanisms for dislocations to climb over obstacles (see Orowan, 1965).

widths result in low resistances to dislocation motion and even the possibility of dissociation of dislocations to produce stacking faults (see Section 4.5).

Figure 4.8 provides a somewhat misleading view of an edge dislocation since the atoms shown are really representative of lines of atoms lying parallel to the dislocation. The individual stretching and bond breaking must take place in coordination with the stretching and distortion of bonds along the dislocation line. For the edge dislocation line to move from one position to another, screw segment kinks form and propagate to enable translation of the dislocation line. As shown in Fig. 4.18, kinks formed on edge or screw dislocations to facilitate glide must have a line direction sense consistent with the glide process.

To this point we have suggested that the applied shear stresses of the type shown in Fig. 4.7 produce motion of a dislocation. To be consistent with the development of stress fields and the elastic energy associated with dislocations, it is essential to have an understanding of how a shear stress produces the virtual force that results in dislocation motion.

Although there are differences in the energies of dislocations that are of edge, screw, and mixed character, the differences are small compared to the affects of changing the length of the dislocation. Formation of a kink or glide step on a glide plane results in a displacement of the material above and below the glide plane at the kink. The magnitude of the force on the element in Fig. 4.18b is simply τb, where τ is the shear stress resolved on the glide plane in the direction of the Burgers vector b. This force arises from doing work W on a unit length of dislocation to move it a unit distance, where

$$F = \frac{dW}{(dsdl)} = \frac{dW}{dA} = \tau b \qquad (4.14)$$

with the terms in this equation[1] defined in Figure 4.18(b).

Thus, we have an energy (or force) corresponding to the length of the dislocation and a force (or energy) required to move a portion of the dislocation that is resisted by the magnitudes of E_{PN} and τ_{PN}.

The examples showing kinked dislocations in Fig. 4.18 exaggerate the nature of a kink by showing sharp corners. Since the energy of a dislocation depends on its length, the energy is often reduced by eliminating those sharp transitions with the inclusion of mixed dislocation segments. The Peierls–Nabarro energy also affects the shapes of kinked dislocations. The minimum energy positions defined by Eq. 4.12 are energy hills that must be overcome to move the dislocation from one valley to the next. Because the dislocation must be continuous and glides by the formation of kinks, the shape of the dislocation will be determined by the magnitude of the energy barrier (see Fig. 4.20). We also know from Eq. 4.9 that increasing the length of a dislocation adds to its energy. Consequently, the shape of the dislocation is controlled by a balance between the position of the dislocation line and minimization of its length. By forming a pair of kinks, a process that is assisted by thermal

---

[1]Remember that by defining this expression "per unit length," this force is scaled to the length or "force per unit length."
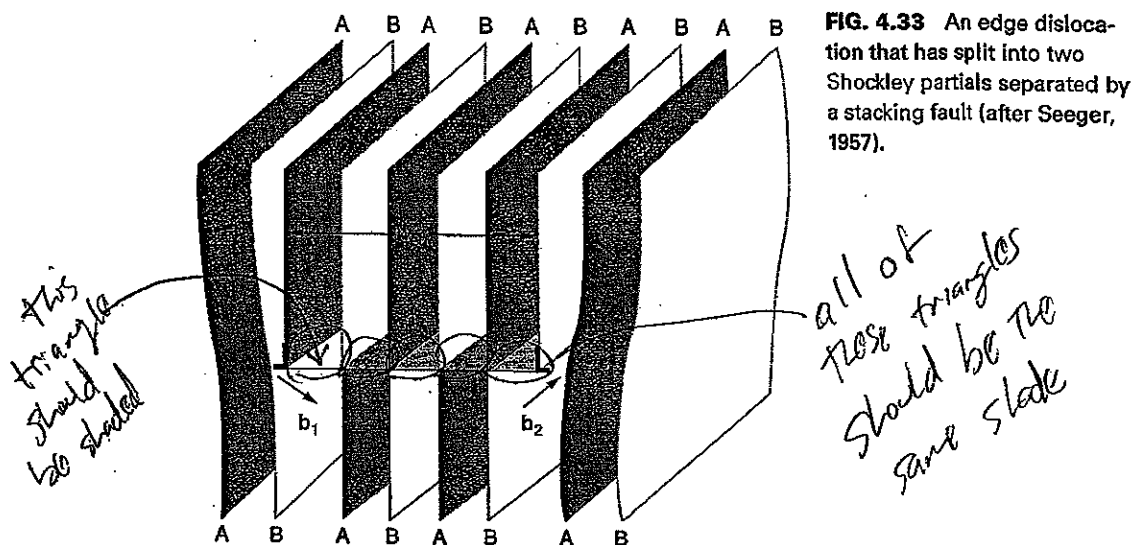
FIG. 4.33 An edge dislocation that has split into two Shockley partials separated by a stacking fault (after Seeger, 1957).

number of FCC metals and alloys. The low-SFE materials have wide stacking faults and inhibited cross slip. Slip in these materials is often coarse, with slip confined to a few planes. The high-SFE alloys toward the bottom of the list cross slip easily and demonstrate finely distributed slip.

EXAMPLE 4.4 *The Widths of Stacking Faults*

We can use Eq. 4.16 to calculate the expected equilibrium widths of stacking faults. We will make a comparison of Ag and Ni using the lowest values given in Table 4.2. We have the following data:

Ag $\qquad$ $SFE = 20 \ mJ/m^2$ $\qquad$ $\mu = 26 \ GPa$ $\qquad$ $b = 2.9 \times 10^{-10} \ m$

$$w_{eq} = \frac{26 \times 10^9 \left(N/m^2\right)\left(2.9 \times 10^{-10} \ m\right)^2}{4\pi\left(20 \times 10^{-3} \ Nm/m^2\right)} = 8.7 \ nm \ (about \ 30b)$$

Ni $\qquad$ $SFE = 130 \ mJ/m^2$ $\qquad$ $\mu = 79 \ GPa$ $\qquad$ $b = 2.5 \times 10^{-10} \ m$

$$w_{eq} = \frac{79 \times 10^9 \left(N/m^2\right)\left(2.5 \times 10^{-10} \ m\right)^2}{4\pi\left(130 \times 10^{-3} \ Nm/m^2\right)} = 3.0 \ nm \ (about \ 12b)$$

4.5.2 Body-Centered-Cubic (BCC) Metals

Slip in BCC metals is easiest in <111> slip directions and has been observed on planes including {110}, {112}, and {123}. The easy slip Burgers vector is $\frac{a}{2}$<111>, which is the closest spacing between atoms in the structure. In contrast with FCC metals wherein the extra half-plane represents two AB plane layers of {110}, the extra half-plane in BCC metals can involve three layers of {111}, as shown in Fig. 4.34. This does allow for some planar spreading of edge dislocations. The nature of the planar spreading differs depending on the plane of slip. The combination of the Burgers vector and the slip plane then specifies the line direction t for edge dislocations lying on different planes. The wide edge dislocation cores for BCC metals enable easy motion of edge dislocations in these materials.

In contrast, $\frac{a}{2}$<111> screw dislocations have cores spread over the threefold symmetry inherent about <111> directions. The spiral of the screw dislocation shows relaxations

4.6 REFERENCES

Dislocations

A. H. COTTRELL, *Dislocations and Plastic Flow in Crystals*, Oxford, 1953.

Dislocations and Properties of Real Materials, The Institute of Metals, 30–50, 1985.

J. FRIEDEL, *Les Dislocations*, Gauthier-Villars, 1956.

J. J. GILMAN AND W. G. JOHNSTON, in *Dislocations and Mechanical Properties of Crystals*, edited by J. C. Fisher, W. G. Johnston, R. Thomson, and T. Vreeland, Jr., Wiley, New York, 116–161, 1957.

P. HAASEN, *Physical Metallurgy*, 2nd Ed., Cambridge, 1987.

R. W. HERTZBERG, *Deformation and Fracture Mechanics of Engineering Materials*, 4th Ed., Wiley, 1996.

J. P. HIRTH AND J. LOTHE, *Theory of Dislocations*, 2nd Ed., Wiley, 1982.

D. HULL AND D. J. BACON, *Introduction to Dislocations*, 3rd Ed., Pergamon Press, 1984.

C. B. JIANG ET AL., *Intermetallics*, 9, 355–360 (2001).

W. G. JOHNSTON, *J. Appl. Phys.*, 33, 2716, 1962.

U. F. KOCKS, A. S. ARGON, AND M. F. ASHBY, *Thermodynamics and Kinetics of Slip*, Progress in Materials Science, Vol. 19, Pergamon Press, 1975.

R. LOW AND R. W. GUARD, *Acta Met.*, 7, 171 (1959).

F. R. N. NABARRO, *The Theory of Crystal Dislocations*, Oxford University Press, 1967.

E. OROWAN, in *The Sorby Centennial Symposium on the History of Metallurgy*, edited by C. S. Smith, Gordon and Breach, 359–376, 1965.

A. SEEGER, in *Dislocations and Mechanical Properties of Crystals*, edited by J. C. Fisher, W. G. Johnston, R. Thomson, and T. Vreeland, Jr., Wiley, New York, 243–329, 1957.

H. SIETHOFF, *Philosophical Magazine*, 82, 1299–1316, 2002.

J. WEERTMAN AND J. R. WEERTMAN, *Elementary Dislocation Theory*, Macmillan, 1964.

BCC Metals and other Materials

A. S. ARGON AND S. R. MALOOF, "Plastic deformation of tungsten single crystals at low temperatures," *Acta Metallurgica*, 14, 1449–1462, 1966.

J. W. CHRISTIAN, *Metall. Trans.*, A14, 1233, 1983.

M. DUESBERY ET AL., *Proc. Roy. Soc.*, A332, 85–111, 1973.

M. DUESBERY, *Proc. Roy. Soc.*, A392, I 145–173, II 175–197, 1984.

V. VITEK, in *Dislocations and Properties of Real Materials*, The Institute of Metals, 30–50, 1985.

4.7 PROBLEMS

A.4.1 Distinguish between a kink and a jog on an edge dislocation (a sketch may help).

A.4.2 Give a first-order estimate of the dislocation density for the crystal shown in Fig. 4.4 in number per square meter.

A.4.3 Describe three examples of dislocations observed in daily life. For each case, provide a sketch and define a Burgers vector. Does each example have a line of dislocation?

A.4.4 Explain the shape of the dislocation etch pits in Fig. 4.10*a* and *b*.

A.4.5 Consider shear stresses applied to the dislocation loop that (a) point to the right above, and to the left below, the loop plane and (b) point up on the left side of the loop and down on the right side of the loop.
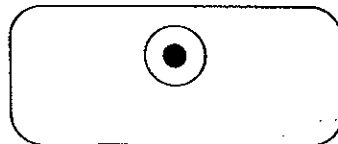
A.4.6 The Burgers vector in the figure below is normal to the plane containing the dislocation loop. Identify with an E or S the character of the dislocation around the loop on all sides. Show the line direction.
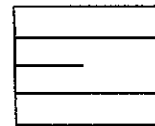
A.4.7 For the dislocation shown in the figure above, show what forces should be applied to the crystal to move the dislocation upward.

B.4.1 Give a numerical estimate with correct units for the energy of a 1-meter-long edge dislocation in MgO.

B.4.2 Single crystals of two different FCC alloys were tested in tension to the same strain. If both specimens were originally the same orientation, explain why one might have slip steps much larger than the other but with a larger spacing between the larger slip steps.

B.4.3 (a) A straight screw dislocation in a BCC metal appears to be 2 μm in length in a TEM micrograph. The direction of the electron beam (normal to the TEM micrograph) was a <113>. What was the foil thickness?

(b) Is there only one possible thickness?

B.4.4 Two Frank–Read sources are operating on the same plane. If a shear stress is applied to operate these two sources, describe the circumstances under which

the loops meeting between the sources would create a larger loop. Assume that cross slip is very difficult. Use detailed sketches. Does it matter if the pinned dislocation segments acting as Frank–Read sources are of the same sign?

B.4.5 (a) An FCC crystal has been deformed by shock loading, resulting in formation of high-energy unit dislocations. Rank order the likely unit dislocations in FCC metals.

$$\frac{a}{2}<100> \qquad a<100>$$
$$\frac{a}{2}<111> \qquad \frac{a}{2}<112>$$
$$a<112> \qquad a<111>$$

(b) Consider a hypothetical $a[100]$ unit edge dislocation in an FCC metal lying on a (010). What is the line direction?

(c) Write a simple partial dislocation reaction for the dislocation in (b), giving a specific example.

(d) Is the partial dislocation dissociation in (c) energetically favorable?

B.4.6 Estimate the force (N) between two parallel straight edge dislocations of opposite sign each 1 m in length at $20b$ away from one another. Explain your answer. (Use $\mu = 100$ GPa and $b = 2.5$ Å.)

B.4.7 If it is assumed that the Burgers vector and elastic properties are about the same for 70–30 brass and copper, which is more likely to undergo cross slip? Justify your answer with a calculation.

C.4.1 (a) Define a $[\bar{1}34]$ crystal with square cross section wherein the front face contains the easy slip direction and the side face is also identified. (b) Find the angle made by the easy slip system on both faces. (c) Find the line direction of edge dislocations for this slip system. (d) Give the line direction of edge dislocations in the second easiest slip system(s). (e) Can

screw dislocations of the first slip system cross slip onto planes of the second?

C.4.2 (a) A BCC crystal contains a dislocation lying at 30° from the ideal line direction for $\frac{a}{2}<111>$ dislocations that lie on a {112} plane. Calculate the energy of this mixed dislocation assuming that $R/r_0 \approx 1000$.

(b) Why might this dislocation lie along this direction?

C.4.3 Describe the intersection of a $\frac{a}{2}[1\bar{1}1]$ dislocation gliding on a $(\bar{2}11)$ plane with a stationary $\frac{a}{2}[\bar{1}11]$ gliding on a $(1\bar{1}2)$ plane in a BCC metal.

C.4.4 A prismatic dislocation with Burgers vector $a[100]$ is present in an NiAl crystal (ordered intermetallic with cubic structure having Ni atoms on corners and Al atoms at the body-centered position). The line segments preferentially lie along <110>. Sketch the loop and give the planes on which these segments can glide. Show how an applied stress could lead to operation of two Frank–Read sources.

C.4.5 A single crystal of aluminum with a $[\bar{1}45]$ compression direction is deformed such that the average dislocation velocity is 1×10^{-7} ms^{-1}. The dislocation density is 10^8 m^{-2}. Estimate the compressive strain rate that would produce such a strain rate. Also give the strengths and weaknesses of any assumptions you have made.

C.4.6 Express Eq. 4.3a–c in terms of stiffness C_{ij}.

C.4.7 Express Eq. 4.3a–c in terms of compliances S_{ij}.

C.4.8 Consider the Orowan equation (Eq. 4.11). If $\rho_\perp$ is considered to increase linearly during straining and the resistance to slip is parabolic with strain, does $\bar{x}$ change?

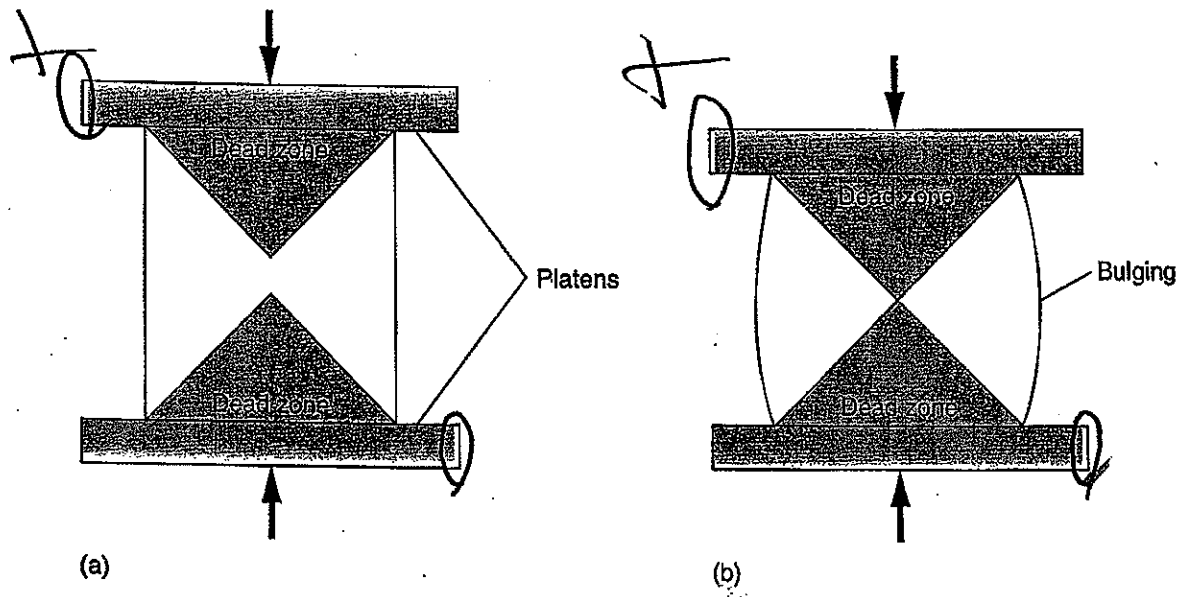**C.4.9** Sketch a process for climb-based dislocation multiplication for compression.

FIG. 5.3 (a) Cross section of compression of a simple right cylinder showing nondeforming dead zones due to friction at the platens. (b) Cross section of the same cylinder after some compression, showing bulging.

gage sections to compression tests can be quite challenging. If frictional coefficients are known, inhibition of deformation by frictional stresses can be modeled using approaches shown in Chapter 10. Friction coefficients usually vary from beginning to end of the deformation. In the ideal case, plastic deformation occurs throughout a part by uniform shear deformation. As shown in Fig. 5.3, friction can result in "dead zones" near the specimen surfaces in contact with the platens. The height-to-diameter ratio of the sample then controls the volume of material deforming to produce a particular magnitude of strain. If the dead zone is a large fraction of the sample volume, the stresses to produce plastic deformation will be exaggerated.

EXAMPLE 5.2 *Constraint During Compression Testing*

The Watts and Ford method (1955) provides an empirical approach for finding a true stress–true strain curve for compression without the influence of end effects. The data obtained by this method also allow for measurement of stress-strain behavior to very large strains without the influence of necking that would occur in a tensile test. Cylinders of equal diameter and different heights are deformed to identical loads. Then, as shown in Fig. 5.4a, the reduction in height can be extrapolated to a diameter-to-height ratio, d/h, with infinite height ($d/h = 0$). Figure 5.4b shows that a reduction in friction through lubrication dramatically affects the strain for a given load. This is not surprising, since the coefficient of friction can be reduced by orders of magnitude by lubrication (see Chapter 9). Problem B.5.6 demonstrates the "strengthening effect" caused by frictional constraint. ∎

The localized stresses of a hardness test are another example wherein constraint can apparently strengthen a material. Figure 5.5 shows a simple model for indentation of a material with a flat indenter. Flow paths of the material in each triangular element are shown by the arrows. If we first consider the deformation as a two-dimensional flow problem, the flow process of the material under the indenter can be separated into the flow regions shown in Fig. 5.5. A dead zone exists below the indenter where the hydrostatic
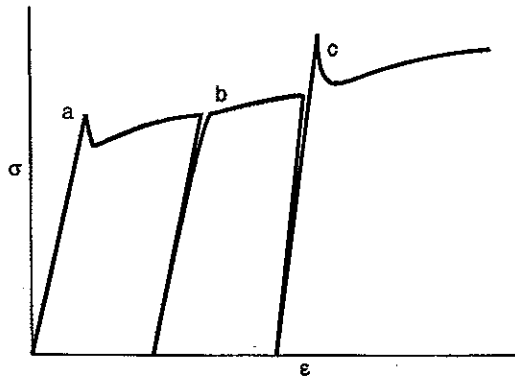
FIG. 5.12 Bake-hardened steels have C and N interstitials that provide strengthening. This strengthening can be enhanced by a heat treatment wherein the C and N diffuse to the dislocations stabilizing their strain fields. This results in a large stress being required for yielding to occur. Three steps of deformation are shown, with (a) representing the initial plastic deformation of a strain aged steel. This material is unloaded and immediately reloaded, as shown at (b). The second loading shows no yield point since the interstitial C and N have had no time to segregate to the dislocations. Strain hardening occurs through multiplication of dislocations. During the next unloading, long times or light heat treatments at 170 to 200°C (bake hardening) can allow for a return of the yield point due to the pinning of the dislocations by strain aging. For each loading, some plastic deformation may precede the upper yield point due to motion of edge dislocations, leading to the impression that the steel has a lower than expected Young's modulus. The lower mobility of screw dislocations and the more effective pinning of them by interstitials leads to formation of the upper yield points. (See the sections on BCC metals in Chapters 4 and 9.)

to denting (Shi, McCormick, and Fekete, 1998). This "strain aging" process can produce increases in yield stress of 20 percent even though the total interstitial alloying content (usually C and/or N) may be less than 0.01 weight percent. The effect of the interstitials is to reduce the mobile dislocation content. To once again get dislocation motion, we must go to a high enough stress level for the dislocations to "break away" from the interstitials. This strengthening is dependent on the time and temperature of the heat treatment. Once they do, the dislocations can move at a much lower flow stress. Tensile stress-strain curves for these materials after strain aging show the type of upper yield point behavior shown for 1020 steel in Fig. 1.19. Figure 5.12 describes the strain aging process as it is applied in bake-hardened steels. ∎

5.2.4 Particulate Strengthening

Precipitation Strengthening Precipitation strengthening (or hardening) is normally much more potent than solution strengthening methods. An understanding of precipitation strengthening incorporates appreciation for nonequilibrium phase changes with dislocation mechanics. Precipitation strengthening is particularly effective in circumstances under which the alloy can be worked into the near final shape before the strengthening treatment. Materials can be shaped at relatively low stresses and then strengthened when at or near the desired dimensions. As shown in Fig. 5.13, the potential increase in strength from controlled precipitation of a second phase can be fivefold or greater. ~~A similarly dramatic example was shown for an aluminum alloy in~~ Fig. 1.21.

Overaging causes a similarly dramatic loss

As might be anticipated by evaluation of Eq. 5.7, the pinning point spacing along the dislocation is critical to strengthening, as is the strength of the pinning obstacle. If these obstacles have a different crystal structure, or just a higher resistance to slip, they can func-

the spacing between the particles decreases as long as the number of particles is increasing. Once the number of particles begins to stop increasing, large particles can grow at the expense of smaller particles. This point also will approximately coincide with the loss of coherency. Incoherent particles will not exert misfit strains and therefore will have a larger limited range of their effects. This stage of aging is called overaging and coincides with a reduction in hardness and strength.

During the time at which the particles are at least partially coherent, dislocations gliding through the alloy matrix can enter and cut through the precipitate, but this requires special relationships between the matrix and the precipitate. The resolved shear stress may also need to be higher than for matrix shear. If the precipitates have become incoherent and far enough apart, the process of bowing leaves dislocation loops around each precipitate as they pass. This leads to synergy between dislocation motion and the precipitates.

EXAMPLE 5.5 *Gamma Prime Ni₃Al in Ni-Base Superalloys*

In nickel-base superalloys, an ordered phase called gamma prime (γ') is used to inhibit plastic deformation. The high oxidation resistance of these alloys, which is derived from passive oxidation of Al and similar compounds, and high strength at high temperatures enable use of these materials in the turbines of jet engines. The γ' is present as precipitates that can be 70 volume percent of the alloy. These precipitates have an ordered structure with a cubic unit cell consisting of Al atoms on the corners and Ni atoms on the faces. Dislocations in the disordered phase move relatively easily. Motion of dislocations in the ordered phase is quite difficult. Each $\frac{a}{2}$<110> dislocation in the disordered phase must pair up with a second dislocation for plastic deformation to occur in the ordered phase, as shown in Fig. 5.16. The longer Burgers and complicated dislocation reactions result in a high critical resolved shear stress, as can be seen in the dislocation velocity versus shear stress data in Fig. 4.21. Unusually, the critical resolved shear stress in this and similar compounds apparently increases with increasing temperature. For this reason, and because of a resistance to diffusion-based high-temperature deformation mechanisms, many nickel-base superalloys have a yield strength that either increases or is almost unchanged with increasing temperature.

Dispersion Strengthening When rigid particles entrained within a metal alloy are not coherent, the strengthening is limited to that attained with the dislocation bowing mechanism with small enhancements from constraint and inhibition of grain growth resulting in strengthening from grain refinement. If the particles have a different thermal expansion coefficient than the matrix, there can also be a strengthening contribution from dislocations formed during cooling from elevated temperatures, but this strengthening contribution is often still less than that from coherency strains between a precipitate and matrix. As discussed in Chapter 6, composites with very fine particulates called dispersion-strengthened alloys provide this type of strengthening and are more stable for high-temperature applications. Larger-scale discontinuous composite reinforcements, platelets, and whiskers, with minimum dimensions of 1 μm, have limited effectiveness
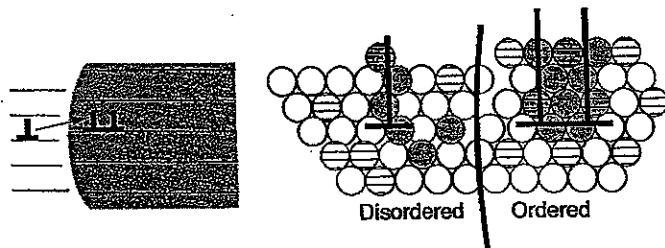

Disordered | Ordered

FIG. 5.16 Passage of a unit dislocation in disordered gamma into ordered gamma prime, resulting in a doubling of the length of a unit Burgers vector.
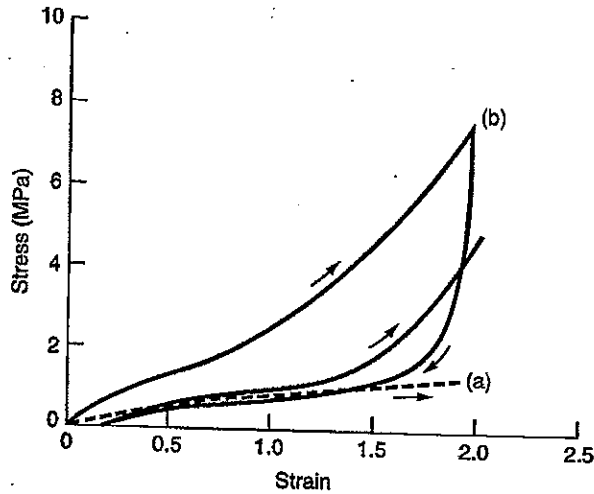
FIG. 5.17 Dispersion strengthening of rubber. (a) Natural rubber without carbon black powder. (b) Natural rubber with 50 percent carbon black powder. (McCrum, Buckley, and Bucknall, 1988, reprinted by permission of Oxford University Press).

in inhibiting dislocation motion since the spacing is large even for high-reinforcement additions. These reinforcements often reside at matrix grain boundaries because they are effective at pinning grain boundaries. These reinforcements do contribute to strengthening by constraint, multiplication of dislocations, and grain refinement, but are not as effective as precipitates distributed throughout a crystal. Filled polymers are another example of dispersion strengthening, as shown in Fig. 5.17. In many plastic parts, powdered metals or ceramics are added to raise the elastic stiffness and also to inhibit plastic deformation by constraining deformation as discussed in Section 5.1

5.2.5 Grain Boundary (or Microstructural Refinement) Strengthening

Control of microstructural scale to produce desired properties is facilitated in most single-phase alloys by static recrystallization and grain growth following introduction of dislocations through cold work. Like the other strengthening mechanisms, justifications describing the fundamentals behind the strengthening are not as convincing as the empirical demonstration. The original expression for grain refinement strengthening is attributed to Hall and Petch with the expression

$$\sigma_{yield} = \sigma_{ini} + kd^{-h} \tag{5.16}$$

where $\sigma_{yield} = Y$, the tensile yield strength, σ_{ini} is the yield strength for a polycrystalline material with infinite grain size (or a hypothetical single crystal of random orientation), k is a proportionality constant, d is the average grain diameter, and h is an exponent of 1/2. Although h can vary from this value, by plotting Eq. 5.16 as σ_{yield} versus $d^{-1/2}$, a rather useful relationship description can be attained, as shown in Fig. 5.18 using expected values for Cu-30Zn brass and copper of commercial purity. Note that, unlike the strengthening expressions given in most cases above, Eq. 5.16 is expressed in terms of normal stresses because the shear stress expressions are not as meaningful if a polycrystal is under consideration. Examples of k-values assuming that $h = 1/2$ are given in Table 5.1. Values of σ_{ini} are not given, because they are strongly dependent on processing history (e.g., cold work and alloy content).

Attempts to represent the basis for this mode of strengthening usually follow one of several approaches. First, because it is not possible except under very special circumstances

In tensile deformation, both materials show a long plastic range with a hardening rate that accelerates with strain. This increasing rate of strengthening is a good indication of chain alignment producing orientation strengthening. Indications of chain orientation are shown by the pole figures in Fig. 5.23, which give an orientation normal to the chain lengths in both materials. The intensity of this preferred orientation increases with strain.

Another aspect of the deformation of PE and PEEK is that each material undergoes a decrease in density (or an increase in specific volume) with tensile deformation, but undergoes almost no density change in simple shear. This shows the effect of dilatant deformation from chain unraveling, lamella fragmentation, and a spreading of chain distances called crazing. Crazing is a dilatant mode of chain spreading observed as whitening at crack tips in some polymers.
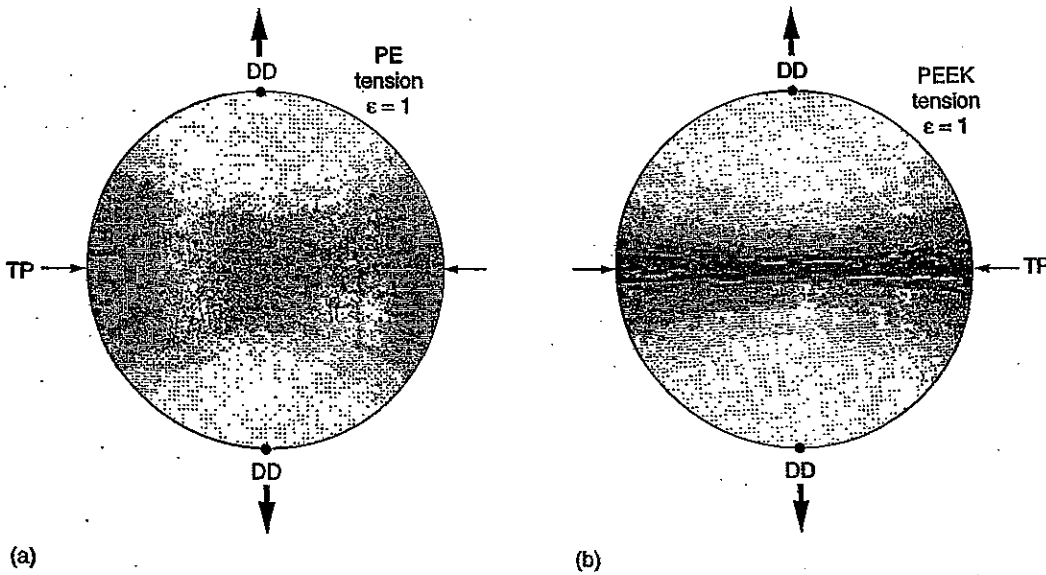

(a)   (b)

FIG. 5.23 Crystalline (200) pole figures of (a) PE and (b) PEEK after deformation in tension for $\varepsilon_{eff} = 1$. The darker the shading, the larger the number of 200 orientations aligned with that direction (G'sell and Dahoun, 1994, reprinted with permission of Elsevier Limited).
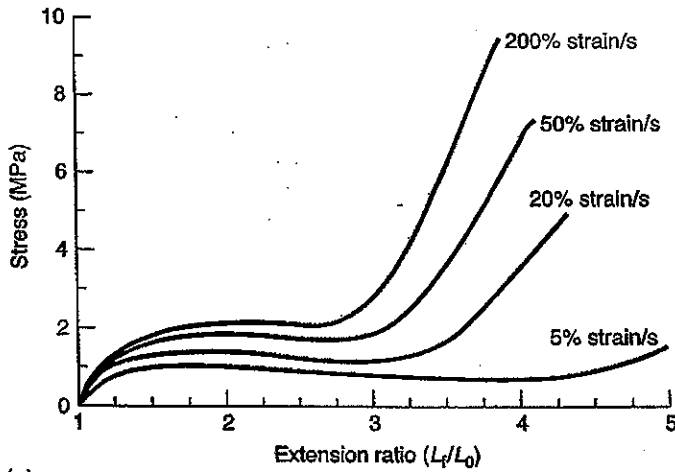
DD is defined as the drawing direction.

(a)

FIG. 5.24 (a) Stress-strain curves for PET specimens stretched biaxially in simultaneous mode at 100°C and at different strain rates (Chandran and Jabarin, I, 1993, Copyright ©This material is used with permission of John Wiley & Sons, Inc.).

requires a tensile stress of 100 MPa, a temperature of 630°C, and a lifetime of 100,000 hr, which is longer than the available data. We can use Fig. 6.3b to see if this particular alloy might be adequate to fulfill the required application in terms of stress rupture behavior. First, we calculate the LMP.

$$LMP = 900 \text{ K}[\log_{10}(100,000) + 20] = 22,500$$

Using this LMP, we can see that the estimated value is about 200 MPa on this log scale. This value would provide a safety factor of only 2 for the given application and would include the uncertainty present in any extrapolation. ■

6.2.2 Monkman–Grant Failure Criterion

Another empirical formulation that is applied to metals and ceramics—the Monkman–Grant failure criterion—employs a power law function of the steady-state creep rate with

$$t_f = A\dot{\varepsilon}_{ss}^{-p} \tag{6.5}$$

where A and p are material-dependent constants. As is evident in Fig. 6.4, the failure strain in ceramics can be inversely proportional to the steady-state creep rate. By reducing the creep rate, the time to failure can be increased. The exponent p is greater than 1 for materials showing this relationship between creep rate and time to failure. If p is equal to 1, the failure strain is independent of the strain rate.

6.2.3 Creep of Polymers

Creep of polymers is quite different from the creep of metals and ceramics described previously (see McCrum, Buckley, and Bucknall, 1988). Many polymers are viscoelastic, which means that although strain may increase with time under a given load, the deformation can, with time, reverse, after the load is removed, to nearly the original dimensions. This can be demonstrated by stretching transparent food storage bags to more than 0.05 to 0.1 plastic strain and then laying them on a table. The bags will continue to undergo visible relaxations for several minutes. At small strains ($\leq 1\%$), viscoelastic creep is nearly linear and can occur at temperatures above 77 K for most polymers. The temperature sensitivity of polymers is quite high. Empirical relations are often applied to extrapolate performance of polymers; however, physical aging processes in polymers that change the molecular structure and uncertainty over accuracy of the extrapolations limit their use in
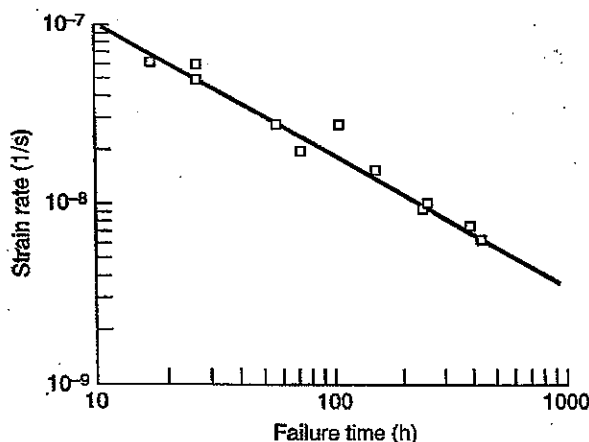

FIG. 6.4 Creep rupture of siliconized silicon carbide with a Monkman–Grant exponent of p = 1.45 (Wiederhorn and Hockey, 1991).
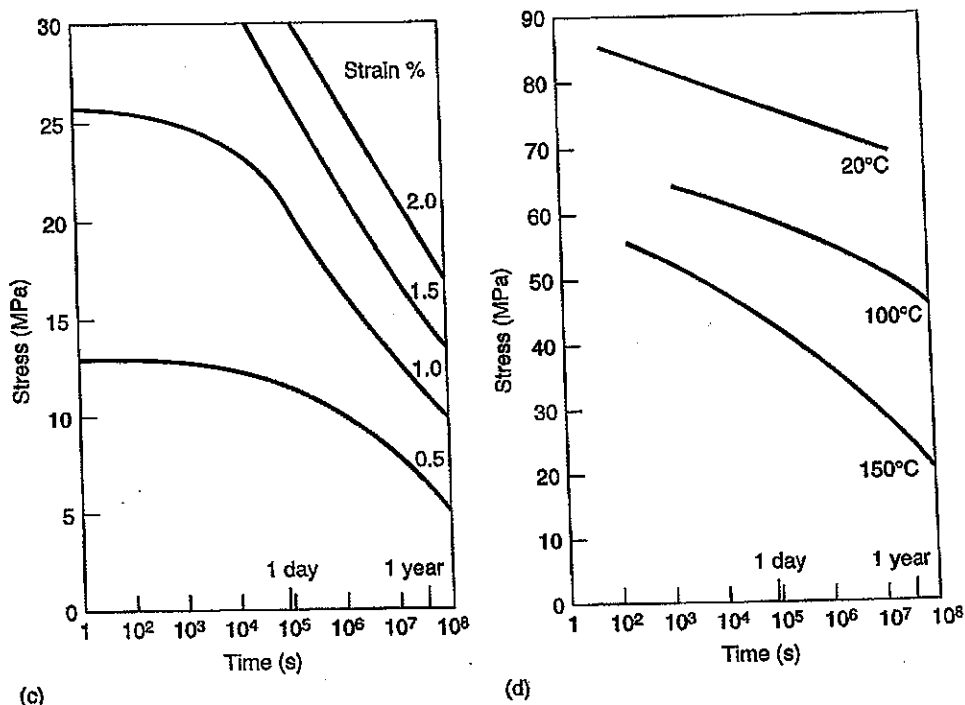
(c)

(d)

FIG. 6.5 (c) Data in (a) replotted at fixed total strain levels. (d) Temperature dependence of failure stress for PES (McCrum, Bucknall, and Buckley, 1988, used with permission of ICI Group).

or fully networked—determine the properties. These materials are often mixtures of very strong intramolecular bonds and relatively weak intermolecular bonds. For both ceramic and polymeric glasses, the density is also a good predictor of the expected mechanical response. The elastic and time-dependent responses both become stiffer or more rigid as the number of bonds per unit volume increases. Figure 6.6 shows the relationship between specific volume (or the inverse of density) and temperature for crystalline, partially crystalline, and noncrystalline glassy materials. Consistent with Fig. 5.14a, there is an abrupt transition in crystalline materials and a gradual transition in glasses. Many glass-forming materials can be at least partially crystallized by holding them just below the melting (or crystallization) temperature for long times. Some polymers and ceramics are specifically designed to
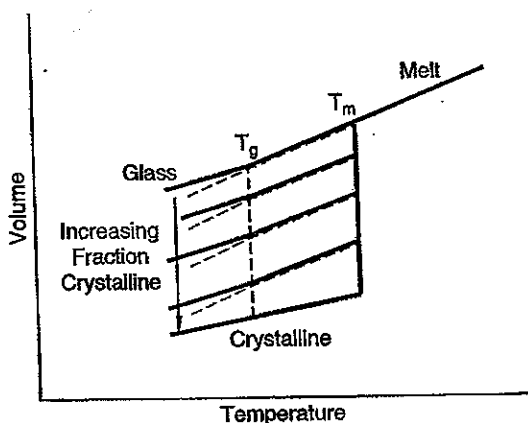
3.24b

FIG. 6.6 Schematic figure showing volume versus temperature for a material that readily forms a glassy structure.

Differences in the glass and crystal volumes are related to the difference in specific volume between the glass and crystal at the glass transition temperature and the temperature dependence of the volumetric thermal expansion difference between the glass and crystal. Then we can write

$$\frac{V_c}{V_f} = \frac{1}{\Delta V_g + 3\Delta\alpha\left(T - T_g\right)} \tag{6.10}$$

where ΔV_g is the volume difference between the glass and crystal forms at the glass transition temperature and $3\Delta\alpha$ is three times the difference in the linear thermal expansion coefficients of the glass and crystal forms. The factor of 3 comes from the isotropic volume strain ($\varepsilon_{vol} = \varepsilon_1 + \varepsilon_2 + \varepsilon_3$) for volumetric expansion. The higher thermal expansion coefficient of the glass arises from the more open intermolecular arrangement.

6.3 STRESS RELAXATION

Stress relaxation (see Fig. 1.14) is a time-dependent response of a material to elastic straining. Because the bonds are stretched elastically, processes of rearrangement within the material can act to relieve elastic stress. The driving force for relaxation processes is simply the elastic energy per unit volume (elastic portion of the area under the stress-strain curve). Stress relaxation tests are conducted by stretching the material to a fixed elastic strain while it is in series with a load cell. The material undergoes stress relaxation as the elastic strain is replaced by plastic strain. The final component deforms at a rate that is driven by a constantly reducing stress. Following stress relaxation, the component has undergone plastic strain corresponding to the reduction in stress.

Stress relaxation is an important process in processing of engineering components. Rapid, nonuniform cooling of components from a high temperature can result in residual stresses. Residual stresses often result from nonuniform cooling or nonuniform deformation of components. Although all of the stresses within a component must balance, the elastic state of the material can vary with position. It is often favorable to induce a state of compressive stress near surfaces to enhance a material's resistance to crack initiation. Many heat treatments, mechanical working processes, and surface treatments are designed to produce this type of strengthening. Unfavorable residual stresses can be relieved by heating the material to a high temperature wherein creep mechanisms are sufficiently active to drive stress relaxation. Glass laboratory equipment or decorative articles made by glass blowers should always be heat treated to relieve internal stresses that might cause premature failure.

Stress relaxation also plays a part in the development of microscale stresses in composites and materials with noncubic crystal structures. As described in Chapter 2, the development of stresses as a result of differences in thermal expansion coefficients can result in stresses between different phases or differently oriented anisotropic grains. The starting point for calculations of residual stresses and internal microscale stresses owing to thermal expansion mismatch is usually a temperature at which the stress relaxation rate is sufficiently high that an assumption is made that the material is uniformly stress-free.

EXAMPLE 6.2 *Tailored Stresses in Glasses*

The resistance of glass to fracture can be improved by producing compressive residual stress on surfaces. This is usually preformed by rapidly cooling the glass surface through the use of air jets. Evidence of heterogeneous cooling is often observable in glasses by photoelastic fringes showing a spectrum of colors corresponding to the stress state of the glass. These fringes are usually visible if
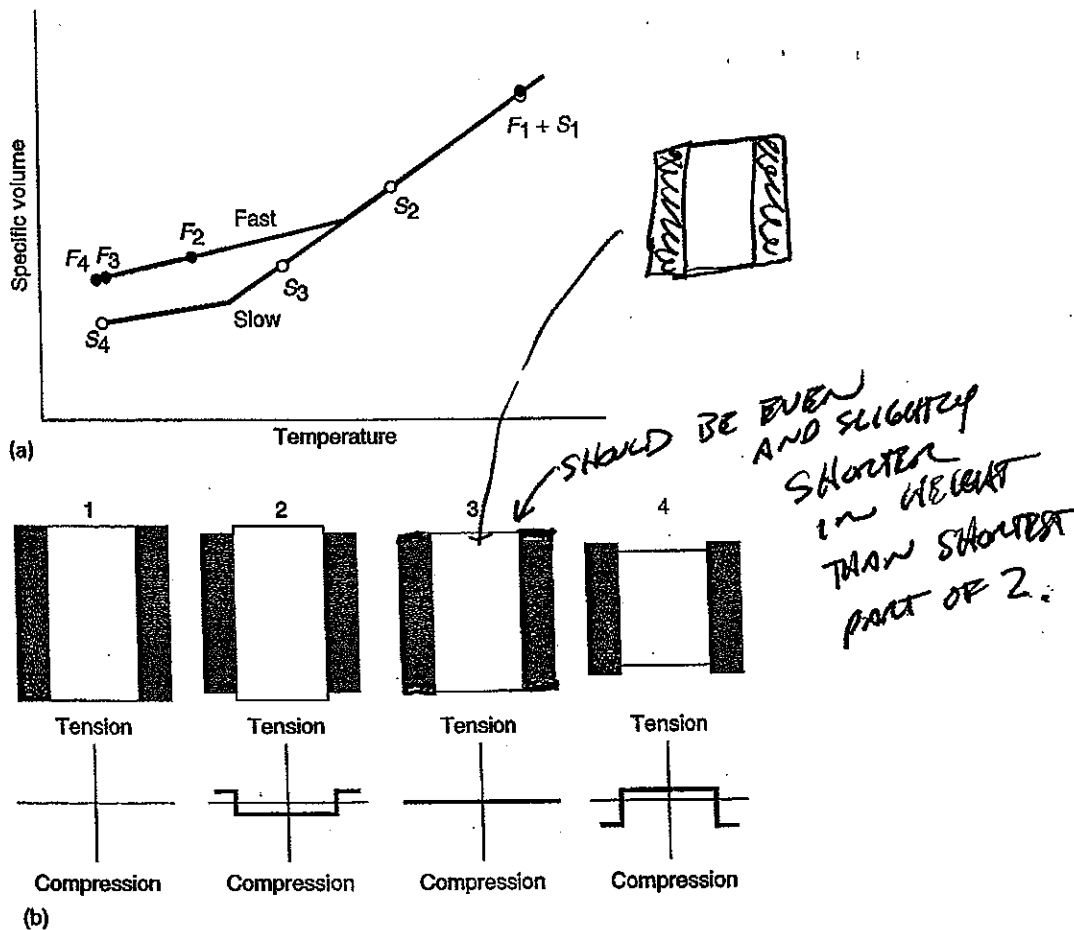
can be performed

(a)

(b)

FIG. 6.8 (a) Specific volume versus temperature relationship for fast cooled surfaces (F) and a slowly cooled interior (S) corresponding to part (b). (b) The fast cooling exterior portion of this section from a glass plate subjected to cooling on both surfaces is shaded. The dimensional changes at sequential times corresponding to part (a) are shown with free displacements in the vertical direction (changes in thickness are not indicated). Schematic stress distributions are shown in the lower segments, with times 1 and 3 being essentially free of internal stresses.

Using residual stresses to improve the fracture resistance of ceramics is a powerful way to improve the performance of glasses and ceramics, but it includes a risk. If the internal tensile residual stresses are very high, deep scratches or damage that reach these internal tensile stresses can trigger dramatic and sometimes hazardous fractures.

you are wearing polarized sunglasses. The presence of compressive residual stress at a surface results in a suppression of crack propagation from surface flaws, which are the most likely initiators of fracture.

Figure 6.8 shows the process undergone by the fast cooled surface (F) and the slowly cooled interior (S) sections of the glass. The subscripts in Fig. 6.8a give the temperature and specific volume for each of the times indicated in Fig. 6.8b. At the start of the process (time 1), the exterior and interior sections are assumed to be stress-free. As the exterior is cooled rapidly, it would prefer to be smaller than the exterior, but the exterior and interior are mechanically coupled so that a stress distribution results

with tension on the fast cooled surface and compression of the interior. The fast cooled material never relaxes to the smaller specific volume possible through slow cooling and remains elastic through the remainder of the cooling process. If the quench is too rapid at this point, the surface is susceptible to fracture. ~~This shows that~~ The quenching rate must be slow enough to avoid fracture at this point.

At time 3, the fast cooled (exterior) and slowly cooled (interior) sections have the same specific volume, which should relax nearly all stresses. This is assisted by the greater potential for relaxation of the slow cooling interior. By time 4, the slow cooling of the interior has resulted in a smaller specific volume than that of the exterior. This differential in specific volumes places the surface in the desired state of residual compression. ∎

6.3.1 Mechanical Analogs for Creep and Stress Relaxation

The time-dependent mechanical responses of many partially crystalline and noncrystalline materials can be accomplished through simple mechanical analogs. The two most common elements for constructing mechanical analogs are springs and dashpots. A spring element is just that, a simple spring constant to describe elastic responses using Hooke's law for a uniaxial response, $\sigma = E\varepsilon$. A dashpot is the damping component in a shock absorber. The mechanical response of a dashpot is directly a viscous response where $\sigma = 3\eta\dot{\varepsilon}$. By assembling springs and dashpots in series (a Maxwell element) or in parallel (a Voigt element), different time-dependent mechanical responses can be modeled. The design of the final model is then related to the expected responses of the strong and weak bonding within the material.

For the Maxwell element, the spring and the dashpot are in series and undergo the same stress, and their strains are additive. The rate equation for the two elements in series is then

$$\dot{\varepsilon} = \frac{d\varepsilon}{dt} = \frac{1}{E}\frac{d\sigma}{dt} + \frac{\sigma}{3\eta} \qquad (6.11)$$

The rate equation for the Voigt element requires the same strain, yielding

$$3\eta\left[\frac{d\varepsilon}{dt}\right] + E\varepsilon = \sigma \qquad (6.12)$$

Table 6.1 shows the separate responses to creep and stress relaxation for each element type.
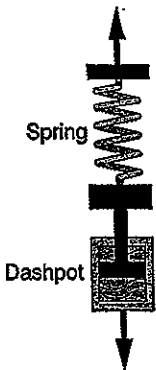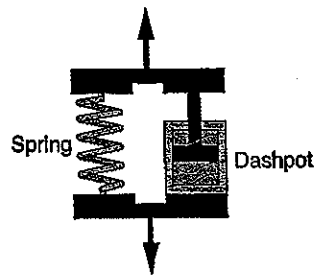
6.3.2 "Jump" Measurements of Time-Dependent Responses

Evaluating the effects of stress and temperature on time-dependent deformation at first appears quite challenging. To recover a complete set of data incorporating the stress dependence and the temperature dependence of the deformation could require extensive testing. With some simplifying assumptions, it is often possible to recover the stress and temperature dependence of deformation for Eq. 6.1 on just one or a fairly small number of specimens. To recover the stress dependence of strain rate, we know that

$$\sigma^{n'} \propto \dot{\varepsilon}$$

where $n' = \frac{1}{m}$ and m is the strain rate sensitivity. If the data are plotted on a log–log plot of strain rate versus stress, the slope of this curve gives the stress exponent n' for individual deformation mechanisms for a number of materials, as shown in Fig. 6.9.

TABLE 6.1 Simple Spring and Dashpot Elements

	~~Voigt~~ *Maxwell*	~~Maxwell~~ *Voigt*
General expression		
Mechanical model	Spring / Dashpot	Spring / Dashpot
Differential equation	$\dfrac{d\varepsilon}{dt} = \dfrac{1}{E}\dfrac{d\sigma}{dt} + \dfrac{\sigma}{3\eta}$	$3\eta\dfrac{d\varepsilon}{dt} + E\varepsilon = \sigma$
Stress relaxation	$\sigma = E\varepsilon e^{-Et/3\eta}$	$\sigma = E\varepsilon$
Creep deformation	$\varepsilon = \dfrac{\sigma}{E} + \dfrac{\sigma t}{3\eta}$	$\varepsilon = \dfrac{\sigma}{E}(1 - e^{-Et/3\eta})$

The stress exponent can also be recovered by performing a temporary "jump" up or down in strain rate, as shown in Fig. 1.**23**, or in stress level, as shown in Fig. 6.10. Assuming that the microstructure is essentially unchanged and there are no adiabatic heating effects, the respective change in stress or strain rate can be used to recover m or n'. The ratio of strain rates is given as

$$\frac{\dot{\varepsilon}_1}{\dot{\varepsilon}_2} = \left(\frac{\sigma_1}{\sigma_2}\right)^{n'} \tag{6.13a}$$

and the ratio of stresses is given by

$$\frac{\sigma_1}{\sigma_2} = \left(\frac{\dot{\varepsilon}_1}{\dot{\varepsilon}_2}\right)^{m} \tag{6.13b}$$

The temperature jump tests (see Fig. 6.11) enable recovery of the activation energy Q_{creep} in Eq. 6.1 for the active creep mechanism by taking a similar ratio of the two strain rates for differing temperatures, where

$$Q_{creep} = \frac{R\ln(\dot{\varepsilon}_1/\dot{\varepsilon}_2)}{1/T_1 - 1/T_2} \tag{6.14}$$

Assumptions included in this include the activity of a single mechanism and no change in the stress exponent. Similar formulations can be used to calculate n' and Q in tensile tests, as shown in Example 6.3.

$$w = \int_0^{\varepsilon_{eff}} \sigma_{eff} d\varepsilon_{eff} \qquad (6.15)$$

If we ignore heat transfer to the surroundings, then the self-heating of a uniformly deformed specimen should be

$$\Delta T \approx \frac{f\int \sigma_{eff} d\varepsilon_{eff}}{\rho C} = \frac{f \bar{\sigma}_{eff} \varepsilon_{eff}}{\rho C} \qquad (6.16)$$

where f is the fraction of stored energy, $\bar{\sigma}_{eff}$ is the average effective stress, ε_{eff} is the total effective strain, ρ is the density, and C is the mass heat capacity in J/(kg·K). Because heat transfer is dependent on time, deformation of materials at high rates can lead to substantial self-heating. Because an increased temperature results in a reduction in the flow stress, deformation instabilities become more likely at higher strain rates. This is particularly true for materials with poor heat transfer properties. Because heat transfer properties decrease with increasing temperature, the susceptibility of materials to localized deformation from self-heating is generally the greatest under hot working conditions. This synergy among self-heating, poor heat transfer, and temperature sensitivity of flow stress makes polymers particularly sensitive to localized deformation.

6.4 CREEP AND RELAXATION MECHANISMS IN CRYSTALLINE MATERIALS

For permanent deformation of a material to take place, a series of critical atomic scale steps must take place. In crystalline materials deforming by dislocation glide, stable kinks must form on dislocations and then the kinks must propagate to advance the dislocation by one Burgers vector. In crystalline materials deforming by dislocation climb, vacancies must move to or from jogs on dislocations to result in deformation strains. In noncrystalline polymers with large molecules, parts of the individual molecules must undergo relative rearrangements that result in an overall displacement. Each of these processes entails a critical step that depends at least in part on the thermal vibrations associated with bonding (see Kocks, Argon, and Ashby, 1975; Weertman, 1968, and Seeger, 1957). The energy that must be employed to overcome barriers determines both the temperature and strain rate dependence of the deformation. Since thermal energy is typically on the order of kT, the increased amplitude of thermal vibrations provides assistance in overcoming activation barriers.

6.4.1 Rate-Dependent Dislocation Glide in Crystalline Materials

The strain rate dependence of slip comes from the Orowan equation in the form

$$\dot{\gamma} = \rho_\perp b \bar{v} \qquad (6.17)$$

and the rate expression

$$\dot{\gamma} = \dot{\gamma}_0 \exp\left(\frac{-\Delta G(\tau)}{kT}\right) \qquad (6.18)$$

where $\bar{v}$ is the average dislocation velocity and $\Delta G(\tau)$ is the stress-dependent activation energy for slip. The value of $\Delta G(\tau)$ is inversely dependent on the shear stress τ. The preexponential term in Eq. 6.18 is

b is the vector magnitude)
Burgers

$$\dot{\gamma}_0 = \rho_\perp b \, s_\perp f_{o\perp} \qquad (6.19)$$

where $s_\perp$ is the average distance swept out by a dislocation for every thermal fluctuation, $\rho_\perp$ is the mobile dislocation density, and $f_{o\perp}$ is the attempt or jump frequency. The local dislocation velocity $s_\perp \cdot f_{o_\perp}$ can be at most the speed of sound in the material. The dislocation jump frequency is a fraction of the vibration frequency $f_{\text{intrinsic}}$, scaled to the ratio of the Burgers vector and the dislocation segment length l by

$$f_{o_\perp} = \frac{b}{l}\left(f_{\text{intrinsic}}\right) \qquad (6.20)$$

For low-temperature deformation of alloys, and particularly in pure BCC metals, the deformation is temperature-dependent. The extent of that temperature dependence is shown by the nearly fivefold change in yield stress for the stress-strain curves of high-purity BCC iron single crystals shown in Fig. 6.14a. The temperature dependence of deformation can be separated into an "athermal" component that scales with the temperature dependence of modulus τ_μ and a component that shows a stronger temperature dependence τ^* with

$$\tau = \tau_\mu + \tau^* \qquad (6.21)$$

In BCC metals, the difficulty in moving screw dislocations provides most of the intrinsic rate dependence for low-temperature deformation. Yield stress data of the type in Fig. 6.14a can be normalized to the temperature-dependent shear modulus to give a relation similar to that shown in Fig. 6.14b.

The stress dependence for the activation energy of deformation can be expressed as

$$\Delta G(\tau) = \Delta G_{o,\gamma} - V^*\tau \qquad (6.22)$$

where V^* is defined as the activation or critical deformed volume. The first term represents the modulus-dependent energy barrier to deformation

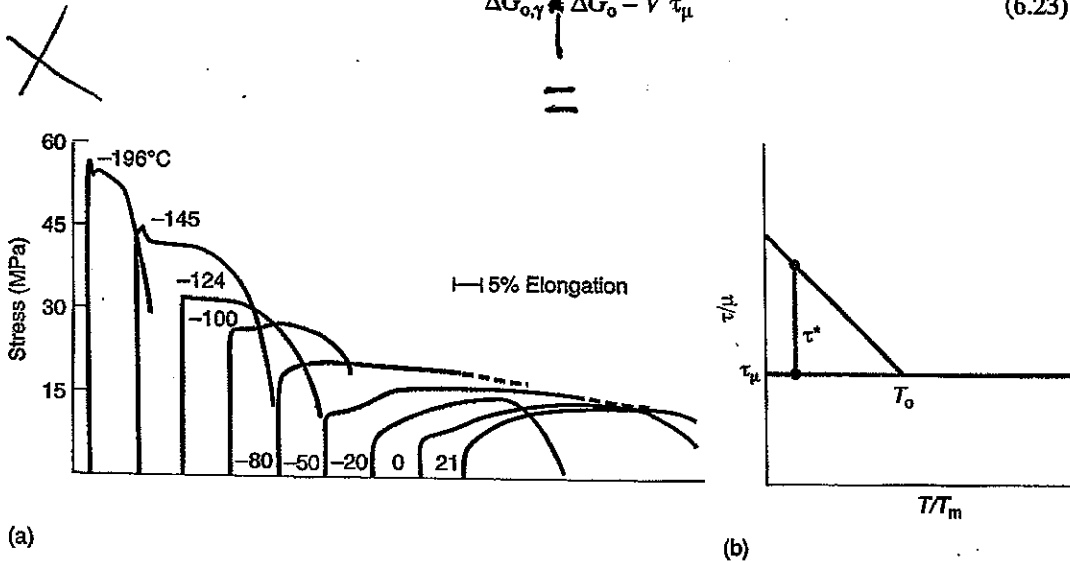$$\Delta G_{o,\gamma} = \Delta G_o - V^*\tau_\mu \qquad (6.23)$$

(a)

(b)

FIG. 6.14 (a) Series of tensile stress-strain curves for high-purity iron crystals with test temperatures given for each curve (after McLean, 1962). (b) Shear stress τ for deformation as a function of temperature normalized to the shear modulus. The terms τ_μ and τ^* indicate the magnitude of the athermal and thermal components of the shear stress. Below a critical temperature T_o, deformation is temperature- and rate-dependent.

which can be substituted into Eq. 6.22 as

$$\Delta G(\tau) = \Delta G_o - V^*(\tau - \tau_\mu)$$

yielding

$$\Delta G(\tau) = \Delta G_o - V^* \tau^* \tag{6.24}$$

The scaling of energy barriers associated with τ^* and τ_μ provides that the barriers associated with τ^* are more localized than those associated with τ_μ. Rearranging the expressions above yields

$$\tau = \tau_\mu + \tau^* \tag{6.25}$$

and substituting for τ^* leads to

$$\tau = \tau_\mu + \frac{\left[\Delta G_o - kT \ln\left(\dfrac{\dot\gamma_0}{\dot\gamma}\right)\right]}{V^*} \tag{6.26}$$

The activation barrier to slip at absolute zero, ΔG_o, is not dependent on strain rate. Below a critical temperature, slip becomes thermally activated and the critical temperature for this transition is strain-rate-dependent. The critical temperature can be given as

$$T_o = \frac{\Delta G_o}{k \ln\left(\dfrac{\dot\gamma_0}{\dot\gamma}\right)} \tag{6.27}$$

In this form, the critical temperature for the transition shown in Fig. 6.14 is strain-rate-dependent, as shown in Figure 6.15.

The strain rate sensitivity can be written as

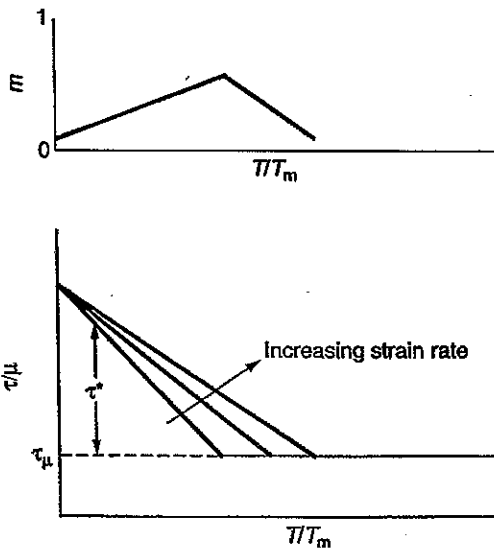$$m = \left(\frac{\partial \ln \tau}{\partial \ln \dot\gamma}\right)_{T, \gamma} \tag{6.28}$$

FIGURE 6.15 The theoretical change in flow behavior with increasing strain rate. The strain rate sensitivity, as inset schematically, is dependent on temperature.

with a fixed temperature T and strain history γ. Figure 6.15 shows that m is a maximum in the vicinity of the critical temperature for experiments conducted at two different strain rates.

An alternative and widely used description of the stress dependence for the slip activation energy (see Kocks, Argon, and Ashby, 1975) is

$$\Delta G(\tau) = \Delta G_o \left[1 - \left(\tau/\tau_R\right)^p\right]^q \tag{6.29}$$

where τ_R is the stress required to overcome obstacles, $\mu b/l$, where l is obstacle spacing. Then, if p and q both equal 1, we get

$$\dot{\gamma} = \dot{\gamma}_o \left(\frac{\tau}{\tau_R}\right)^{\Delta G_o/kT} \tag{6.30}$$

which is equivalent to an expression for power law creep (see next section)

$$\dot{\gamma} \propto \tau^{n'} \tag{6.31}$$

For a range of obstacle spacings and obstacle geometries, the constants for dislocation glide fall into the ranges

$$0 < p < 1$$
$$1 < q < 2 \tag{6.32}$$

The obstacle strengthening strain rate expression can be given as

$$\dot{\gamma} = \dot{\gamma}_o \exp\left[\frac{\Delta G_o}{kT}\left(1 - \frac{\tau}{\tau_R}\right)\right] \tag{6.33}$$

with

$$\dot{\gamma}_o = \alpha \left(\frac{\tau}{\mu}\right)^2 f_{o_\perp} \tag{6.34}$$

where α is a constant that depends on dislocation arrangements. For strong obstacles, the stress dependence of $\dot{\gamma}_o$ in Eq. 6.34 can be set as a constant from 10^5 to 10^6/s. Table 6.2 shows the relative values of ΔG_o and τ_R for different types of obstacles.

TABLE 6.2 Strengthening Components in Eq. 6.33 (after Frost and Ashby, 1982)

Obstacle strength	ΔG_o	τ_R	Example
Strong	$2\,\mu b^3$	$> \dfrac{\mu b}{l}$	Strong precipitates
Medium	0.2–$1\,\mu b^3$	$\approx \dfrac{\mu b}{l}$	Dislocations
Weak	$< 0.2\,\mu b^3$	$\ll \dfrac{\mu b}{l}$	Solution strengthening

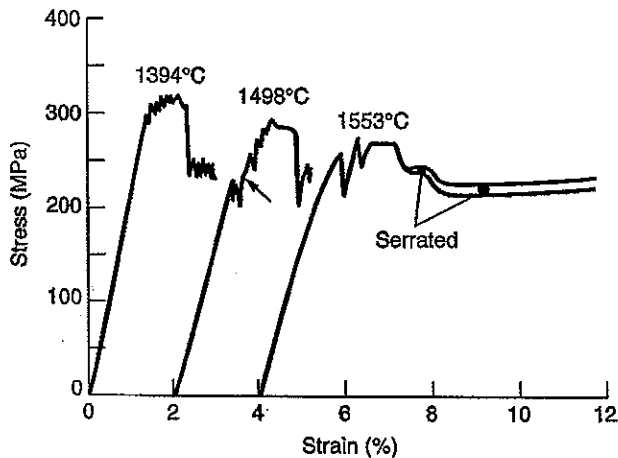**FIG. 6.17** Compressive stress-strain behavior of <112> oriented single crystals of a 3.4 weight percent Y_2O_3-ZrO_2 alloy. The deformation is very serrated, indicating difficulty in initiating dislocation multiplication and twinning. Also, because these are compression tests, the low plastic strains before failure suggest that tensile deformation might show little or no plasticity for similar strain rates (Muñoz, Wakai, and Dominguez-Rodriguez, 2001, with permission of Elsevier Limited).

{100} planes because of the reduced symmetry. The stress levels for deformation at these temperatures are comparable to room-temperature values for many high-strength polycrystalline metal alloys, but it should be remembered that pure zirconia melts at about 2800°C. Although transmission electron microscopy results confirm that some dislocation motion has occurred in the compression tests shown in Fig. 6.17, some twins are also present in the specimens. ■

EXAMPLE 6.5 *Anomalous Yield Behavior in Ni₃Al Intermetallics (γ')*

The nickel-aluminum intermetallic called γ'(Ni₃Al) has an unusual dependence of yield stress on temperature. Unlike most other materials, over a wide range of temperatures the yield stress of metal compounds with this structure increases to a maximum. This phenomenon is shown for two different γ' single-crystal orientations in Fig. 6.18. The yield stress increase continues over a wide range of temperatures until reaching a maximum between 800 and 1000°C. Precipitates with this structure are those found in nickel-base superalloys, suggesting one way in which superalloys are able to resist creep so well at high temperatures. The ordered structure of Ni₃Al, which is cubic with nickel atoms on the faces of a unit cell and aluminum atoms on the corners, constrains slip into dislocation pairs, as suggested by the TEM micrograph shown in Fig. 4.38. The dislocations that produce the deformation slip on the <101> {111} system, but the Burgers vector length of the dislocations $\frac{1}{2}$<101> only displaces the nickel atoms in the aluminum sites. This means that the order of the intermetallic will be locally interrupted (or out of phase). To be a unit dislocation, it must go from one aluminum atom to another or from one nickel atom to another. The two $\frac{1}{2}$<101> dislocations (Fig. 4.38) added together return the perfect structure. These dislocations also move differently for tensile and compressive deformation, and this difference is orientation-dependent, as can be seen in Fig. 6.18. The deformation behavior after the maximum becomes strongly influenced by the power law creep mechanisms discussed in the next section and slip on other slip systems is also observed. ■

6.4.2 Power Law Creep

For creep, the steady-state, stage 2 strain rate is often used as a basis for creep mechanisms. The strongly sloped portions of the creep curves in Fig. 6.9 show power law creep (PLC) for several materials. Between $0.3T_m$ and $0.6T_m$, metals and ceramics often show a strong dependence on strain rate, consistent with Eq. 6.30 and 6.31. In this intermediate temperature regime and at high stresses, deformation occurs by a combination of glide and diffusion. The power law exponent n' in Eq. 6.31 can range from 3 to 10. The lower range of 3 is determined by the combination of a low value of ΔG_o in Eq. 6.33 and the preexponential factor in Eq. 6.34. For low ΔG_o, the applied stress in the exponential has a linear stress
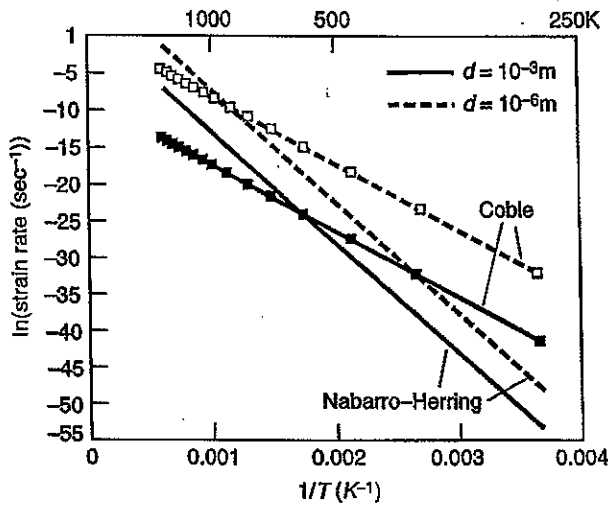
FIG. 6.21 Relationship between strain rates for Nabarro–Herring and Coble creep as a function of T for two grain sizes. The Nabarro–Herring creep curve is plotted without symbols, and the Coble creep curve is indicated by square symbols.
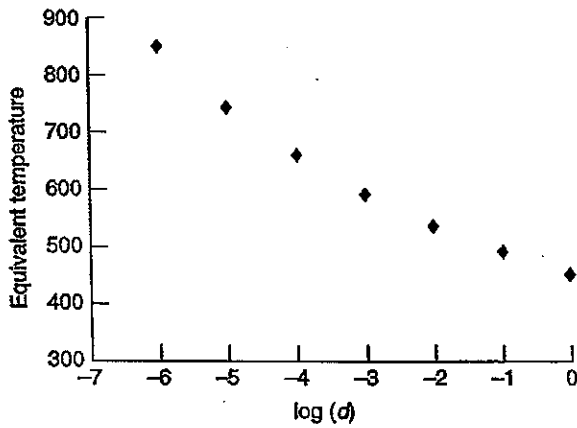

FIG. 6.22 Relationship between grain size and the temperature at which $\dot{\varepsilon}_{NH} = \dot{\varepsilon}_C$.

For a constant stress, the point at which the Nabarro–Herring and Coble creep rates are equal as a function of grain size and temperature can be obtained by a plot of the type shown in Fig. 6.21.

Figure 6.21 shows that decreasing grain size results in higher strain rates for both Nabarro–Herring and Coble creep. Also, the temperature at which $\dot{\varepsilon}_{NH} = \dot{\varepsilon}_C$ increases with increasing temperature. Or, in other words, Coble creep is dominant to higher temperatures with decreasing grain size (as long as grain growth is not occurring). This relation can be determined explicitly by setting $\dot{\varepsilon}_{NH} = \dot{\varepsilon}_C$ and solving for the two variables d and T. For the Germanium data, this yields

$$T(d) \cong \frac{13,800}{30 + \ln(d)}$$

This is plotted in Fig. 6.22. These relations between deformation rates for different mechanisms are employed in Chapter 8 to create deformation mechanism maps.   ■

6.4.4   Grain-Boundary Sliding

To inhibit formation of internal voids, material must be transferred at the grain boundaries. Raj and Ashby (1971) suggested that the rate of grains sliding past one another under shear stress is determined by the grain-boundary shape. The sliding process consists of a relative
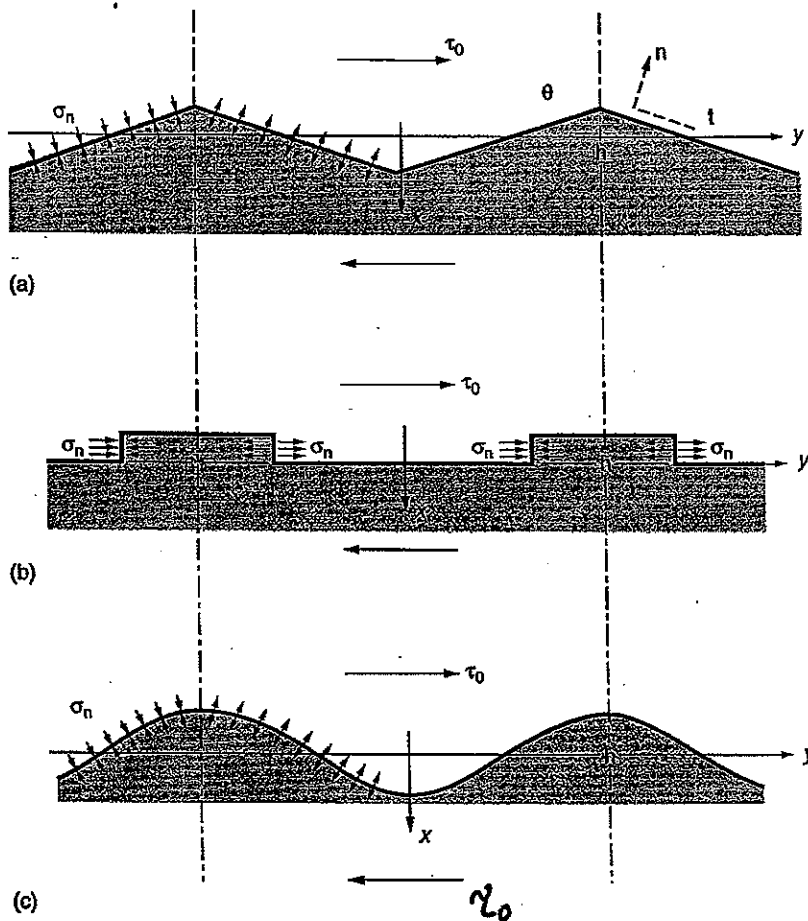
FIG. 6.23 The application of a shear stress τ_0 results in normal stresses acting between grains with (a) sawtooth, (b) step, and (c) sinusoidal boundaries. The normal stresses between the grains at this plane are labeled σ_n (Raj and Ashby, 1971, used with permission).

displacement of the individual grains, but a pictorial image of grains skating past one another should be avoided. Grain-boundary sliding (GBS) experimental observations on Cu and Ag bicrystals have shown that specimens from the same bicrystal vary in creep resistance, grain-boundary migration changes creep resistance, hard precipitates slow GBS, and the activation energy for GBS is often equivalent to that for lattice diffusion.

The microscopic steps on boundaries between two crystals are shown in Fig. 6.23. A shear stress is applied across the boundary with an atomically smooth interface separated by a viscous fluid. For crystalline materials without a grain-boundary phase, the high transport rates near the boundary effectively provide such a condition, and many ceramics with a glassy grain-boundary phase possess such interfaces. For this case, the sliding rate between the two crystals is given by the effective viscosity of the grain-boundary phase. For rough interfaces, the sliding process must be accommodated by strains at the rough interface similar to those found in friction and wear processes.

The accommodating strains can be elastic or plastic. In the elastic case, once the stresses at the contact points are sufficiently high, the sliding process arrests. Plastic deformation at this interface can occur by dislocation motion at high stresses and low temperatures. At high temperatures, the local tensile and compressive stress gradients result in

(b) Plot the ratio of dA/dt for a necked area versus the unnecked area of a tensile bar for $m = 0, 0.2, 0.5, 0.8$, and 1. Discuss your results.

B.6.3 Make a schematic plot of molar volume versus temperature for a given glass as a function of the macromolecule size using a range of curves spanning easy crystallization to difficult crystallization.

B.6.4 Two different types of mechanical testing equipment are commonly used: those that apply a force through a hydraulically actuated cylinder and those that apply a displacement by rotating screws that move the grips apart. Which type of equipment would be best for conducting a creep test, and which would be best for conducting a stress-relaxation test? Explain your answer.

B.6.5 A series of strain rate jumps (up and down) are given in Fig. 1.23 for polyurethane. Estimate the strain rate sensitivity of the polyurethane material.

B.6.6 Describe why the temperature rise for the same deformation of aluminum conducted at two different temperatures, say 100 and 200°C, might be different. Which temperature would give the greatest temperature rise for the same deformation?

B.6.7 Plot the activation energies for self-diffusion given in Fig. 6.19 versus melting temperature by estimating the values and looking up the corresponding melting temperatures. From this plot, estimate the activation energies for creep of Mo and Ag.

B.6.8 Plot the creep behavior of a Maxwell element that is placed under a load of 10 MPa for 1000 sec and then under no load for 1000 sec. The Maxwell element has the following properties:

(a) $E = 10$ GPa, $\eta = 5$ Pa/sec
(b) $E = 10$ GPa, $\eta = 100$ Pa/sec
(c) $E = 100$ GPa, $\eta = 5$ Pa/sec
(d) $E = 100$ GPa, $\eta = 100$ Pa/sec

[handwritten: 0.5 MPa·sec, 10, 11, 0.5, 11, 10]

B.6.9 Plot the creep behavior of a Voigt element that is placed under a load of 10 MPa for 1000 sec and then under no load for 1000 sec. The Voigt element has the following properties:

(a) $E = 10$ GPa, $\eta = 5$ Pa/sec
(b) $E = 10$ GPa, $\eta = 100$ Pa/sec
(c) $E = 100$ GPa, $\eta = 5$ Pa/sec
(d) $E = 100$ GPa, $\eta = 100$ Pa/sec

[handwritten: also here]

B.6.10 Plot the stress relaxation behavior of a Maxwell element that is stretched to a tensile strain of 0.1 and held at that length. The Maxwell element has the following properties:

(a) $E = 10$ GPa, $\eta = 5$ Pa/sec
(b) $E = 10$ GPa, $\eta = 100$ Pa/sec
(c) $E = 100$ GPa, $\eta = 5$ Pa/sec
(d) $E = 100$ GPa, $\eta = 100$ Pa/sec

[handwritten: also here]

B.6.11 Plot the stress relaxation behavior of a Voigt element that is stretched to a tensile strain of 0.1 and held at that length. The Voigt element has the following properties:

(a) $E = 10$ GPa, $\eta = 5$ Pa/sec
(b) $E = 10$ GPa, $\eta = 100$ Pa/sec
(c) $E = 100$ GPa, $\eta = 5$ Pa/sec
(d) $E = 100$ GPa, $\eta = 100$ Pa/sec

[handwritten: also here]

C.6.1 How can Eq. 6.36 be obtained from the Orowan equation and Eq. 6.35?

C.6.2 Why is a low stacking fault energy material likely to undergo dynamic recrystallization?

C.6.3 Estimate the maximum tensile residual stress for a rod of a material that consists of a fast cooled surface that remains glassy while the interior crystallizes. Assume that $\Delta V_g = 0.01$, $\alpha_{glass} = 10 \times 10^{-6}$ C^{-1}, $\alpha_{crystal} = 5 \times 10^{-6}$ C^{-1}, $(T - T_g) = 400$°C, and $E_{glass} = E_{crystal} = 150$ GPa.

C.6.4 Derive a relationship for strain rate in two Maxwell elements in parallel. Assume that the material constants (E and η) are identical in both Maxwell elements. Plot strain versus time and stress versus time for creep and stress relaxation of the two parallel elements, and compare these plots with the proportional behavior of a single Maxwell element.

C.6.5 Derive a relationship for strain rate in a Maxwell element and a Voigt element in series. Assume that the material constants (E and η) are identical. Plot strain versus time and stress versus time for creep and stress relation. Explain each transition.

C.6.6 If you found strain rate jump tests to give different values of strain rate sensitivity at different temperatures, what would you give as the possible reasons?

C.6.7 The data given in the following table are based on the original data given by Grant and Bucklin (1950, used with permission of ASM International), for alloy S-816. Convert the data to appropriate units and plot graphs similar to Fig. 6.3a and b, finding your best value for the constant C. How does this data set compare with that used in Fig. 6.3a and 6.3b?

B.7.7 Take a half-sheet of paper and fold it on its diagonal. Use a pair of scissors to cut a notch perpendicular to the fold. Open the fold, and you have an angled notch that should result in a mixed-mode geometry. Grasp the ends of the paper and pull it in tension until it fails. What combination of modes did the initial notch represent? By what mode(s) did the final fracture propagate? Explain this result.

C.7.1 Write the Mode I stress distributions (Table 7.2 or above) in Cartesian coordinates.

C.7.2 Write the Mode II stress distributions in Table 7.2. in Cartesian coordinates.

C.7.3 Write the Mode III stress distributions in Table 7.2 in Cartesian coordinates.

C.7.4 Write the Mode I displacement distributions in Table 7.2 in Cartesian coordinates.

C.7.5 Write the Mode II displacement distributions in Table 7.2 in Cartesian coordinates.

C.7.6 Write the Mode III displacement distributions in Table 7.2 in Cartesian coordinates.

C.7.7 If the formation of a process zone is based only on dilation (volume increase), what would you expect to happen to the process zone size in a thick specimen (how would it compare with Fig. 7.12)?

C.7.8 Determine the relative shapes of the plane stress contours for the plastic zone using the Tresca criterion. This will require use of a spreadsheet, a program, or math software.

C.7.9 A volcano has erupted on your small coastal island and you know it is urgent to move all of your belongings. The capacity of the steel bridge that connects you to the coast is about that of your truck even before you load it. Unfortunately, you have noticed a crack freshly initiated by an earthquake associated with the volcano. The crack is in a primary load-bearing span of the bridge. It looks bad. Helicopters and boats are not an option. What could you do to reduce the risk of the bridge collapsing when you drive across it? You have very little time, but a good set of tools (and safety glasses).

C.7.10 Toughening of brittle materials has been accomplished by transformation toughening. The toughening is accomplished through the effects of the transformation strains—the differences in unit cell dimensions before and after transformation. Discuss the effectiveness of the following transformation strains in producing toughening in both plane stress and plane strain conditions. (Also see Chapter 3.)

(a) $\varepsilon_T = \begin{vmatrix} 0.04 & 0 & 0 \\ 0 & -0.04 & 0 \\ 0 & 0 & 0 \end{vmatrix}$

(b) $\varepsilon_T = \begin{vmatrix} -0.04 & 0 & 0 \\ 0 & -0.04 & 0 \\ 0 & 0 & 0.01 \end{vmatrix}$

(c) $\varepsilon_T = \begin{vmatrix} 0.01 & 0.04 & 0 \\ 0.04 & 0.01 & 0 \\ 0 & 0 & 0.02 \end{vmatrix}$

C.7.11 Find the stress contour for 101 MPa for plane strain conditions using the data in Example 7.2 and the values of f given in Table 7.2. Compare your result with that given in Example 7.2.

C.7.12 Use the von Mises criterion to determine the value of r at which the elastic stress solution will reach a yield stress of 2 MPa at $\theta = 0$ for the data in Example 7.2. Give solutions for both plane stress and plane strain conditions.

C.7.13 The fracture surface of a failed bolt shows that a small half-penny crack has formed at the bottom of one of the threads. First make a sketch of the fracture surface, and then use superposition to calculate the failure load given the following data:

The thread: $D = 5$ mm, $d = 4$ mm, $K_{Ic} = 18$ MPa $\sqrt{m}$

The half penny: $a = 0.08$ mm

C.7.14 Pete the glass blower spits on a small notch he has made in glass to make a cleaner break before applying a bending load. What is so special about Pete's saliva that makes the glass fracture easier? (It works!)

C.7.15 For an infinite thin plate with a center crack with a length of $2a = 8$ cm and a stress of 10 MPa: (a) Calculate the principal stresses at

$(r,\theta) = 1$ µm, 30°

100 µ, 30°

1 µm, 45°

100 µm, 45°

1 µm, 60°

100 µm, 60°

1 µm, 90°

100 µm, 90°

(b) Which points will exceed the Tresca yield criterion assuming that $Y = 200$ MPa?

(c) Show the "orientations" of the principal stresses.

EXAMPLE 8.1   *Deformation Mechanisms in Ice*

Consider uniaxial loading of ice at −50°C and a compressive stress of 10 MPa. We use Eq. 3.20:

$$\tau_{eff} = \sqrt{\frac{(10)^2 + (10)^2}{6}} = 5.8 \text{ MPa}$$

To get the actual value of the stress ratio on the y-axis in Fig. 8.2, we need the shear modulus of ice at that temperature. We can see that at the solidification temperature the shear modulus of ice is about 1 MPa/3 × 10⁻⁴ ≈ 3 GPa. At a temperature of −50°C, we expect the modulus to be higher, so we can expect that it might range from 3.7 to 3.3 GPa. This estimate fits pretty well with the data in Table 8.1. The corresponding ranges are shown on the DMM with resulting shear stress ratios of 1.5×10^{-3} to 1×10^{-3}. The expected effective shear strain rate is then $\dot{\gamma}_{eff} \approx 10^{-7}/s$. Then, using Eq. 8.1 and the Levy–von Mises relations, we can calculate the principal strain rates as follows:

$$\frac{\dot{\varepsilon}_1}{-10 - \frac{1}{2}(0+0)} = \frac{\dot{\varepsilon}_1}{-10} = \frac{2}{9}\left(\frac{10^{-7}}{5.8}\right) \qquad \varepsilon_1 = -3.8 \times 10^{-8}/s$$

$$\frac{\dot{\varepsilon}_2}{0 - \frac{1}{2}(-10+0)} = \frac{\dot{\varepsilon}_2}{5} = \frac{2}{9}\left(\frac{10^{-7}}{5.8}\right) \qquad \dot{\varepsilon}_2 = \dot{\varepsilon}_3 = 1.9 \times 10^{-8}/s$$

■

Research on ice is conducted by scientists and engineers who study motion of the polar ice caps and glaciers. High pressures and high homologous temperatures can lead to significant creep rates, and dynamic recrystallization is often part of the deformation seen in glaciers.
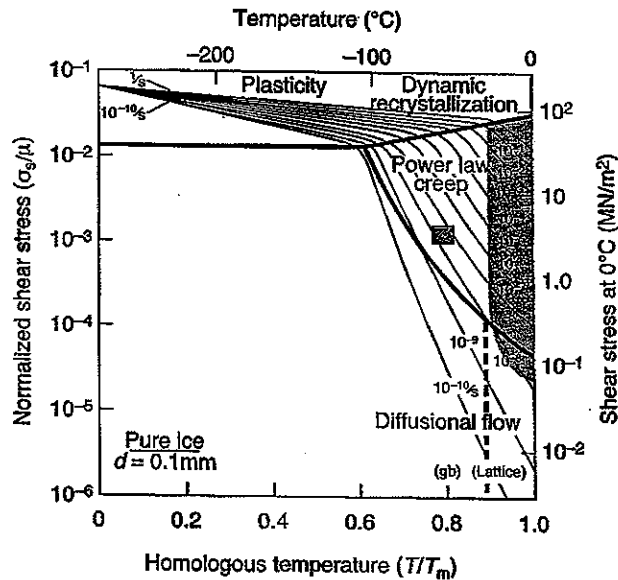
FIG. 8.2 Plot of normalized stress level versus homologous temperature of ice with a 0.1-mm grain size. Ice shows a very high resistance to deformation just below its melting temperature. The highly directional character of its bonding imparts this high strength relative to its elastic constants. The small gray square inset represents the range of deformation conditions discussed in Example 8.1 (Frost and Ashby, *Deformation Mechanism Maps,* Pergamon Press, New York, 1982, with permission).

The positions of some boundaries in DMMs depend strongly on microstructure, with dislocation density affecting glide and climb and grain size having a significant effect on diffusion creep mechanisms. The effects of grain size and dislocation density on nickel with commercial purity are shown in Fig. 8.3. In Fig. 8.3, increasing grain size in a work hardened material results in strong decreases in the diffusional creep rates, expanding the regime of stresses and temperatures over which power law creep is the dominant mechanism. In the first of these materials, shown in Fig. 8.3a, the small (1 mm) grain size results in a diffusional flow regime in which boundary diffusion (Coble creep) is the dominant diffusion-based mechanism nearly to the melting temperature. Because Eq. 6.33 is used for dislocation glide, the obstacle spacing resulting from prior work hardening has an effect. For this and all subsequent DMMs, where appropriate, the obstacle spacing, l, is given in the caption. Figure 8.3c shows that a distinctly separate range of boundary diffusion can be separated from lattice diffusion (Nabarro–Herring creep) at a grain size of 1 mm. The position of this transition between dominant regions for Coble creep and Nabarro–Herring creep is determined using the same procedure as that shown in Example 6.5. Figure 8.3d,
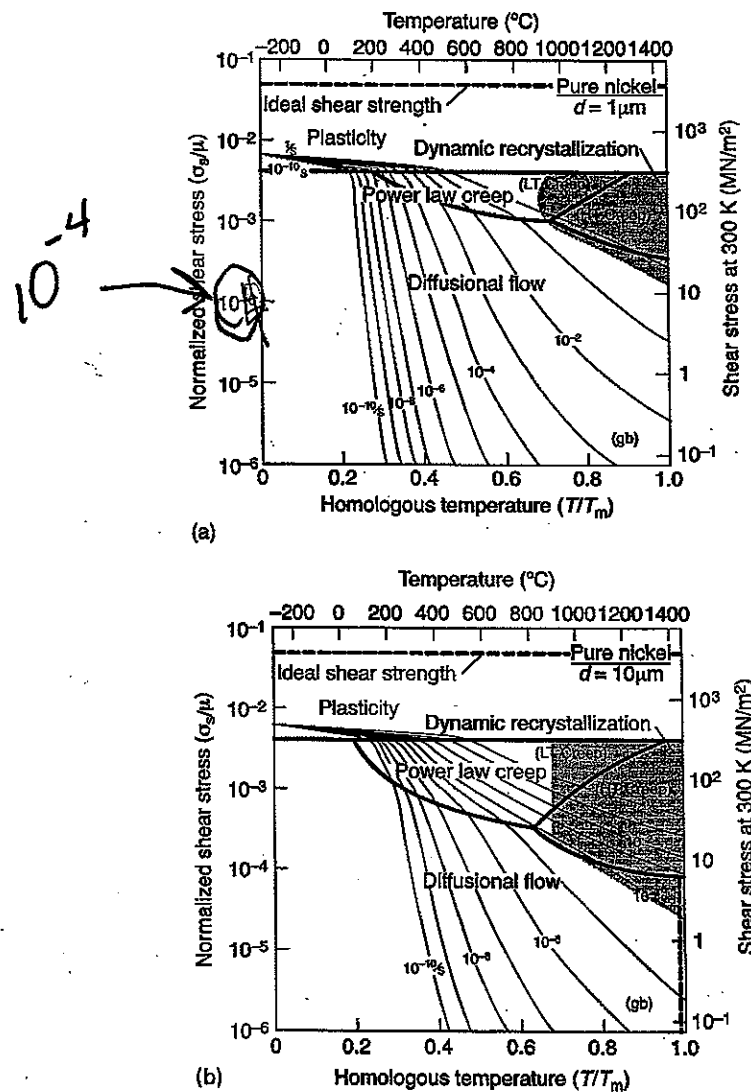

FIG. 8.3 DMMs for pure nickel with grain sizes of (a) 1 μm and (b) 10 μm with a work hardened obstacle spacing of $l = 4 \times 10^{-8}$ m (Frost and Ashby, *Deformation Mechanism Maps*, Pergamon Press, New York, 1982, with permission).
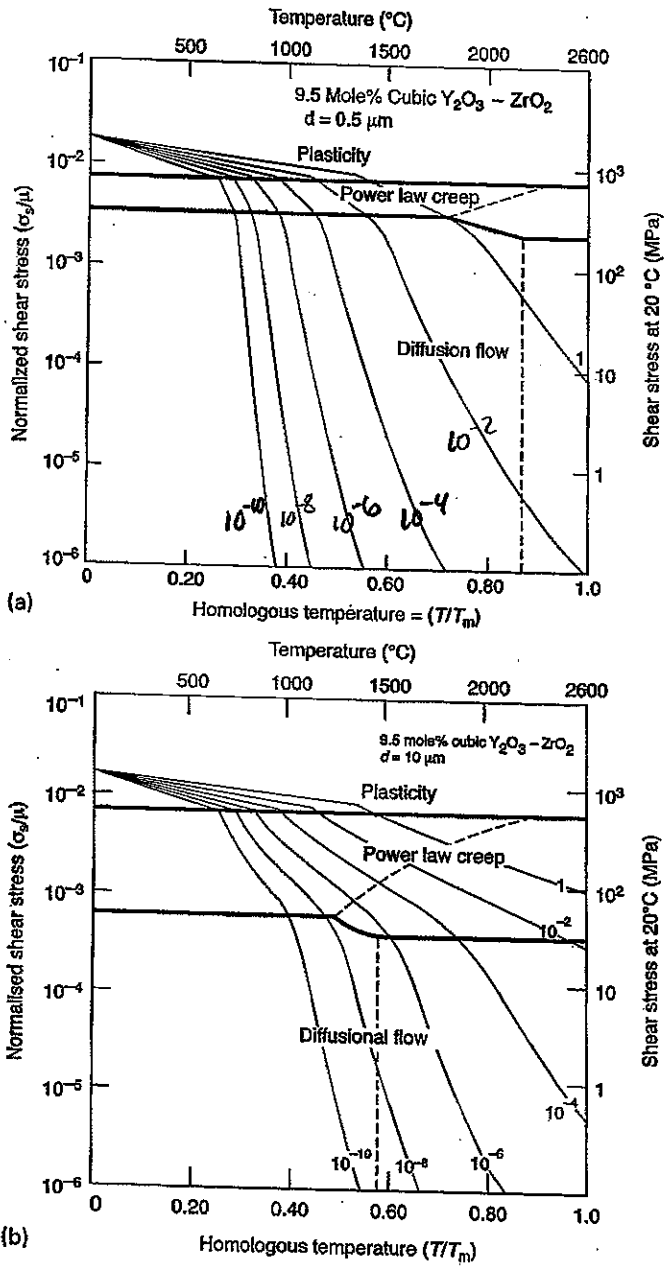
...ticity shows almost no dependence on strain rates ...icity in a polycrystal are fairly high owing to the limited number of slip systems. In contrast, the regimes over which power law creep is the dominant deformation mechanism are quite large. Recrystallization also occurs over a relatively wide range of stresses and temperatures.

For polycrystalline silicon, it is clear in Fig. 8.7b that the highly covalent diamond cubic crystal structure does not readily enable slip at low stresses and also that diffusion contributions to deformation are very sluggish. In fact, many of the features of the DMM for silicon are similar to the example for ice shown in Fig. 8.3. In ice, the highly directional bonding between individual water molecules and the associated difficulty of diffusion of the water molecules through the ice result in a material that is substantially resistant to plastic deformation even near its melting temperature. Although Si is an element, the directional-

FIG. 8.7 DMMs for (a) the close-packed hexagonal metal zinc with a grain size of 0.1 mm, (b) the diamond cubic material silicon with a grain size of 100 µm and the strain rate contours given in logarithms of base 10. (Frost and Ashby, *Deformation Mechanism Maps*, Pergamon Press, New York, 1982, with permission).

(a)

FIG. 8.8 DMMs for grain sizes of (a) 0.5 μm and (b) 10 μm for a ceramic alloy consisting of yttria and zirconia. The composition was chosen so that considerations of phase transitions that would be present at other compositions would not be necessary. (DMM constructed by Purdue MSE 555 students Duan, Elsner, Oppong, and Vest, 1993)

(b)

nia alloys have been extensively investigated, this example of an estimated DMM can be constructed as described here. The data used for the generation of the zirconia maps are given in Table 8.2 along with the references and relevant equations from Chapter 6.

The temperature dependence of the shear modulus comes from data by Kandil et al. (1984), who reported shear moduli for yttria-containing crystals at 293 K and at 973 K. For each temperature, the shear modulus is linearly extrapolated to the composition 9.5 mole percent yttria. These values suggest a dimensionless temperature-dependent coefficient ($d\mu/dT$) of 0.72 if we assume that the change in shear modulus with temperature is essentially linear. The activation energy for plasticity reported by Dominguez-Rodriguez et al. (1986) for the alloy 9.4 mole percent Y_2O_3–ZrO_2 is nearly three times larger than the activation energies for lattice resistance controlled plasticity used by Frost and Ashby (1982) for ThO_2 and UO_2, so this should have a significant influence on the DMM of

10.1 IDEAL ENERGY APPROACH FOR MODELING OF A FORMING PROCESS

The ideal energy approach relies on a very basic energy balance wherein the applied work is set equal to the deformation energy (see Wagoner and Chenot, 1997). No friction effects or heterogeneous deformation are considered in this model of a forming operation, so we can consider the process a lower bound. No die geometry is considered in this model of deformation. Simple tensile deformation of a reduced section that is well away from the enlarged heads wherein the material is gripped can be considered an ideal process. The work per unit volume conducted in a tensile test can be described as

$$w_{ideal} = \int_0^{\varepsilon_{eff}} \sigma_{eff} d\varepsilon_{eff} \qquad (10.5)$$

where the effective strain $\varepsilon_{eff} = \ln(A_{final}/A_{initial})$. If we use the power law hardening expression introduced in Eq. 3.19, the ideal work is then

$$w_{ideal} = \frac{K\varepsilon_{eff}^{n+1}}{n+1} \qquad (10.6)$$

We can apply this ideal concept to forward extrusion, as shown in Fig. 10.10. Then the amount of work applied per unit volume can be related to the extrusion pressure by $P_e > w_{ideal}$. Similarly, the minimum stress required to pull the material through the dies in drawing is σ_d, leading to $\sigma_d > w_{ideal}$. Some simple corrections can be made to evaluate the deformation efficiency of an actual process, but these mostly consist of factors that are better evaluated by the techniques given in Sections 10.2 and 10.3.

EXAMPLE 10.2   *Calculation of the Ideal Drawing Stress*

A rod of an aluminum alloy has been reported to have a strain hardening behavior given by $\sigma_{eff} = 350\varepsilon_{eff}^{0.3}$ (MPa). We would like to calculate the expected drawing stress if the aluminum alloy is to be reduced from an original diameter of 15 mm to 13 mm. First we would like to find the effective strain, which is given by

$$\varepsilon_{eff} = 2\ln\frac{15}{13} = \cancel{0.143} \qquad 0.286$$

If we apply this strain in Eq. 10.6 we can write

$$w_{ideal} = \frac{350(0.143)^{1.3}}{1.3} = 21.5 \text{ MPa} = 21.5 \times 10^6 \frac{J}{m^3} \qquad \blacksquare$$
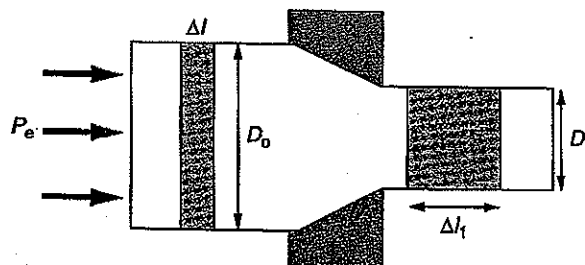

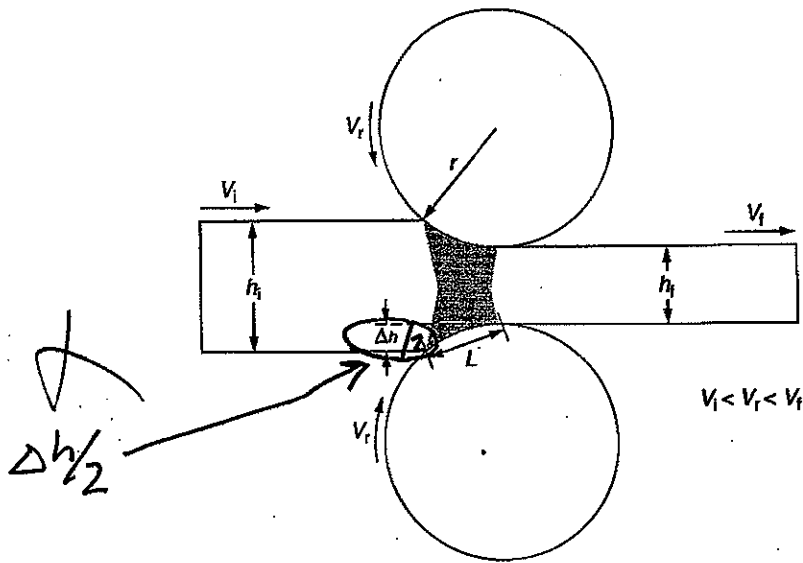**FIG. 10.10**   Schematic figure showing extrusion of a round cross section and the changes in shape for a selected element.

FIG. 10.1 Detailed rolling geometry showing two rolls moving in opposite directions to deform a slab of material to a height reduction of Δh. The approximate contact length of the rolls is L. As shown in this diagram, the plastic deformation takes place principally in the *roll bite*, which is shaded gray. The increase in velocity from the entrance to the exit is shown along with the intermediate velocity. $V_i < V_r < V_f$

The contact length for the near plane strain compression conditions in the *roll bite* is given by the approximation $L \cong \sqrt{r \Delta h}$, as shown in Fig. 10.1. About midway in this length is a single position, called the neutral point, that indicates the line of contact wherein the roll surface velocity v_r is equal to the velocity of the material. The transition in relative velocities is shown in Fig. 10.2*a*. Because of the relative motion of the material with respect to the rolls, the frictional forces develop as illustrated in Fig. 10.2*b*, which shows a pressure maximum at the neutral point along what is called the *friction hill*. The friction hill can be described by the pressure function

$$P_{\text{roll}} = \frac{h}{\mu_F L}\left(\exp\frac{\mu_F L}{h} - 1\right)\sigma_0 \tag{10.1}$$

where h is the average height of the material in the roll bite, $(h_i - h_f)/2$, μ_F is the frictional coefficient (discussed in Chapter 9), and σ_0 is the average plane strain flow strength, $2k$, or the shear yield strength as defined by the Tresca relationship discussed in Chapter 3. If work hardening is considered, the value of the average flow strength is just $(2k_{\text{initial}} + 2k_{\text{final}})/2$, where $2k_{\text{initial}}$ is the initial flow strength and $2k_{\text{final}}$ is the strength following the rolling process. The deformation in the roll bite is nearly plane strain owing to the constraint provided by the material before and after the material within the roll bite, as shown in Fig. 10.3 and demonstrated in Example 10.1.
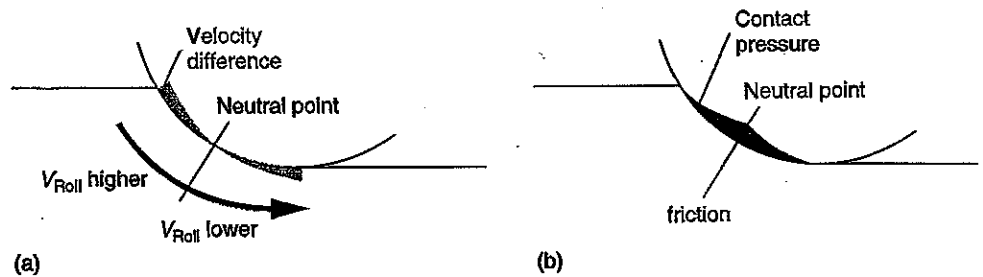

FIG. 10.2 (a) Schematic velocity differentials and neutral points in the roll bite. (b) Schematic pressure differentials along the roll–material contact length.